EXPERIMENTAL AND THEORETICAL INVESTIGATION OF CONTACT RESISTANCE AND RELIABILITY OF LATERAL CONTACT TYPE OHMIC MEMS RELAYS

Except where reference is made to the work of others, the work described in this thesis is my own or was done in collaboration with my advisory committee. This thesis does not include proprietary or classified information.

____

Lia Almeida

Certificate of Approval:

____
Robert Jackson
Assistant Professor
Mechanical Engineering

____
Ramesh Ramadoss, Chair
Assistant Professor
Electrical and Computer Engineering

____
Stuart M. Wentworth
Associate Professor
Electrical and Computer Engineering

____
Joe F. Pittman
Interim Dean
Graduate School

Experimental and Theoretical Investigation of Contact Resistance and Reliability of Lateral Contact type Ohmic MEMS Relays

Lia Almeida

A Thesis

Submitted to

the Graduate Faculty of

Auburn University

in Partial Fulfillment of the

Requirements for the

Degree of

Master of Science

Auburn, Alabama
December 15, 2006

EXPERIMENTAL AND THEORETICAL INVESTIGATION OF CONTACT RESISTANCE AND RELIABILITY OF LATERAL CONTACT TYPE OHMIC MEMS RELAYS

Lia Almeida

Permission is granted to the Auburn University to make copies of this thesis at its discretion, upon the request of individuals or institutions and at their expense. The author reserves all publication rights.

____

Signature of Author

____

Date of Graduation

THESIS ABSTRACT

EXPERIMENTAL AND THEORETICAL INVESTIGATION OF CONTACT RESISTANCE AND

RELIABILITY OF LATERAL CONTACT TYPE OHMIC MEMS RELAYS

Lia Almeida

Master of Science, December 15, 2006
(B. S., Auburn University, 2003)

81 Typed Pages

Directed by Ramesh Ramadoss

In this thesis, the reliability of electrostatically actuated ohmic contact type MEMS relays has been investigated. Multi-contact MEMS relays using electrostatic comb-drive actuators have been used in this study. The MEMS relays were fabricated using MetalMUMPs process, which uses 20 μm thick electroplated Nickel as the structural layer. A 3 μm thick gold layer was electroplated at the electrical contact surfaces. The overall size of the relay is approximately 3 mm x 3 mm. The relay consists of a movable main beam anchored to the substrate using two identical folded suspension springs. RF ports consist of five movable fingers connected to the movable main beam and six fixed fingers anchored to the substrate. Comb-drive actuators located at the top and bottom ends of the main beam enable bi-directional actuation of the RF contacts. An example MEMS relay with planar contacts of area 80 μm x 20 μm and a spacing of 10

μm between the movable and fixed contacting surfaces is discussed. Resistance versus applied voltage characteristics has been studied. For an applied DC bias voltage of 172 V, the movable fingers make contact with the fixed fingers. The resistance versus applied voltage characteristics have been measured for applied bias voltages in the range of 172 V to 220 V. Reliability testing has been carried out and the resistance variation of the MEMS relay over 1 x 10^6 actuation cycles has been measured. A statistical rough surface contact model was used to estimate the actual electrical contact resistance versus applied force curve of these devices. Two models were presented, the Greenwood and Williamson (GW) elastic model, and the Jackson and Green (JG) model. When compared to the measured results, the GW model over estimates the resistance, but the JG model is very accurate. A multi-scale contact model is also presented, and the results show good qualitative agreement with the experimental data.

ACKNOWLEDGEMENTS

I would like to thank my advisor Dr. Ramesh Ramadoss, for his help, patience and guidance in successfully choosing a topic and completing my Masters Degree requirements. Thanks also to Dr. Robert Jackson and Dr. Koji Ishikawa for their help with this project.

Thanks to my parents and family in Brazil for supporting me, and for always being there when I needed. Also, thanks to my host family, Larry and Becky, whom without I would not be here in the first place. Most specially, thanks to Estevam, who has always been there to support me, even when my decisions did not agree with his.

Thanks to all my friends who have come and gone, who are far and close, and are too many to name.

I would also like to sincerely thank the ECE Staff, specially Charles, William, Linda B., Les, Joe, Robert Dean, Mike Palmer, for all their indirect help in achieving my research objectives. Thanks to my colleagues, Ananth, Ron, Brian, Madhu, Roger, Drew, and Shakib.

Style manual of journal used Graduate School: Guide to preparation and submission of theses and dissertations

Computer software used Microsoft Office XP

TABLE OF CONTENTS

LIST OF FIGURES ….…………………………………………………...……....x

LIST OF TABLES ..………………………………………………………..…........xiii

CHAPTER 1 INTRODUCTION AND OVERVIEW 1

CHAPTER 2 MEMS RELAY DESIGN..4

2.1 Introduction...4
2.2 MEMS Relay Configuration...4
2.3 MEMS Relay Design 6
2.3.1 Comb Drive Design 6
2.3.2 Folded Suspension Spring Design 8
2.4 MEMS Relay Simulation...10
2.4.1 Boundary Conditions 11
2.4.2 CoSolve Results..12
2.5 MEMS Relay Fabrication 13
2.5.1 MetalMUMPs Design Rules...13
2.5.2 MetalMUMPs Fabrication Process 14
2.5.2.1 Process Steps..15

CHAPTER 3 EXPERIMENTAL CHARACTERIZATION 22

3.1 Experimental Setup...22
3.2 Resistance vs. Voltage Characteristics 23
3.2.1 Resistance versus Applied Voltage for Other Contact Geometries..........................25
3.3 Reliability Study 26
3.3.1 Stiction 26
3.3.2 Lifetime Testing..28
3.3.3 Reliability Test of Contact Geometry E..30
3.4 MEMS Relay Packaging..31
3.4.1 Package Selection 32
3.4.2 Wire Bond Arrangement...34
3.4.3 Printed Circuit Board 35
3.4.4 Packaging Details...36

CHAPTER 4 MEMS RELAY CONTACT MODELING 40

4.1 Greenwood and Williamson elastic contact model...41
4.2 Jackson and Green elasto-plastic hemispherical contact model 43
4.3 Multi-scale model 45

4.3.1 Asperity Electrical Contact Resistance 47
4.4 Results and Discussion 48

CHAPTER 5 SUMMARY AND FUTURE WORK 52

5.1 Summary 52
5.2 Design, Simulation and Fabrication 52
5.3 Experimental Characterization and Packaging 52
5.4 Modeling 53
5.5 Future Work 53

BIBLIOGRAPHY 55

APPENDICES 60

APPENDIX A AMSTC MEMS RELAY FABRICATION 61

A.1 Introduction 61
A.2 Design 61
A.2.1 Mask Design 62
A.3 Fabrication Process 63
A.4 CONCLUSION 68

LIST OF FIGURES

Figure 2-1 Multi-contact MEMS relay using comb-drive actuators (a) open state, and (b) closed state 5

Figure 2-2 Comb drive actuator structure....6

Figure 2-3 Basic folded suspension spring design schematic....8

Figure 2-4 Schematic for folded suspension spring derivation 9

Figure 2-5 MEMS relay 3D meshed model of the MEMS relay used for simulation in Coventorware....10

Figure 2-6 CoventorWare model of the MEMS relay showing various boundary conditions....11

Figure 2-7 Displacement versus Applied Voltage characteristics for the MEMS relay....12

Figure 2-8 Cross section of MetalMUMPs process showing various layers....14

Figure 2-9 Step 1 in the fabrication of the MEMS relay using the MetalMUMPs process (a) top view, and (b) cross section. 15

Figure 2-10 Step 2 in the MetalMUMPs process step 2 (a) top view, (b) OXIDE 1 mask layout, and (c) cross section of the oxide 1 layer. 16

Figure 2-11 Step 3 in the MetalMUMPs process (a) top view, (b) NITRHOLE mask layout, and (c) cross section of the nitride layer. 16

Figure 2-12 Step 4 in the MetalMUMPs process (a) top view, (b) METANCH mask layout, and (c) cross section of the oxide 2 layer....17

Figure 2-13 Step 5 in the MetalMUMPs process (a) top view, (b) METANCH mask layout, and (c) cross section of the metal layer....18

Figure 2-14 Step 6 in the MetalMUMPs process , (a) METAL mask layout, and (b) cross section of the metal layer....18

Figure 2-15 Step 7 in the MetalMUMPs process (a) top view, and (b) cross section of the contacts....19

Figure 2-16 Step 8 in the MetalMUMPs process (a) top view, (b) GOLDOVP mask layout, and (c) cross section....20

Figure 2-17 Step 9 in the MetalMUMPs process (a) top view, and (b) cross section. 20

Figure 3-1 Experimental setup for testing the MEMS relay (a) Schematic Block diagram, (b) photograph of the setup....23

Figure 3-2 Measured resistance versus applied voltage characteristics of the MEMS relay....25

Figure 3-3 MEMS relays contact geometries....25

Figure 3-4 Comparison of average measured resistance versus applied voltage characteristics for MEMS relays with four different contact geometries as shown in Figure 3-3....26

Figure 3-5 Stiction of the movable finger to the fixed fingers in the MEMS relay with Type A contact design....27

Figure 3-6 Resistance versus applied voltage characteristics before and after dehydration for MEMS relay with Type A contact design....27

Figure 3-7 MEMS relay resistance degradation over actuation cycles for actuation voltage applied to (a) the top comb-drive actuator, and (b) bottom comb-drive actuator....29

Figure 3-8 SEM picture of the RF contact in the MEMS relay (a) a movable finger located between the top and bottom fixed fingers in the open state, (b) side wall of the RF contact surface at the start of the reliability test, and (c) side wall of the RF contact surface after $8x10^5$ actuation cycles....30

Figure 3-9 Resistance degradation over actuation cycles for the MEMS relay with Type E contact design....31

Figure 3-10 Package details from the specification sheet provided by Spectrum Semiconductor Materials (a) top view, pad layout, (b) bottom view, pin layout, and (c) connection table....33

Figure 3-11 Chosen lid for packaging the MEMS relay (a) schematic, and (b) lid photograph....34

Figure 3-12 Chip schematic containing nine MEMS relays (a) chip pad labels, and (b) wire bonding schematic....35

Figure 3-13 Printed circuit board for testing the packaged MEMS relay (a)Printed circuit board top view, (b) socket for the packaged relay, and (c) PCB along with the socket....36

Figure 3-14 Package containing wire bonded MEMS relay (a) before glass lid sealing (b) after glass lid sealing....38

Figure 3-15 Lid placement run profile used for the SST International 3150....39

Figure 4-1 Suface data for MEMS relay contact surface acquired using the Wyco optical profilometer....48

Figure 4-2 SEM picture of the contact surface of the MEMS relay a) contact finger showing 1 μm thick gold electroplated on nickel, and b) a portion of the finger showing the rough gold contact surface on nickel....49

Figure 4-3 Comparison between the GW and the JG models for contact area versus load....50

Figure 4-4 Comparison between the GW, JG models, and measured results for ECR versus load 50
Figure 4-5 Comparison between the Hertz and JG multi-scale models and measured results for the MEMS relay....................51

Figure A- 1 AMSTC fabrication masks for multi-contact design, (a) PADS, (b) ANCHOR, (c) NICKEL, and (d) all mask levels combined....................62
Figure A- 2 AMSTC fabrication masks for single-contact design, (a) ANCHOR, (b) NICKEL, and (c) ANCHOR and NICKEL levels combined. 63
Figure A- 3 A 4" Wafer after Ti/Cu seed layer deposition....................65
Figure A- 4 The anchor openings in the 1045 photoresist....................65
Figure A- 5 Close up view of anchor openings shown in Fig A-4. 66
Figure A- 6. SU-8 mold for for plating the switch 67
Figure A- 7. Electroplated nickel switches after removal of SU-8. 68
Figure A- 8 Suggestion to avoid nickel platting under SU-8....................68

LIST OF TABLES

Table 2-1 Design parameters for the comb drives and the folded springs.........................10

Table 2-2 Mask level names, minimum features and minimum space for each mask level in the MetalMUMPS process. 13

Table 2-3 Design Rules between layers in the MetalMUMPS process. 14

Table 3-1 Part number and description of package and lid purchased from Spectrum Semiconductor Materials, Inc (www.spectrum-semi.com). 32

Table 3-2 Relationship between chip pad, package pad, and package pin. 35

Table 3-3 Palomar 2460-IV settings for wire bonding of MEMS relay chip 37

Table 4-1 Material and surface properties for MEMS relay 49

CHAPTER 1 INTRODUCTION AND OVERVIEW

Microelectromechanical Systems (MEMS) is a technology that combines mechanical and electrical functions in a single device with feature sizes ranging from millimeters to micrometers. A great advantage of MEMS is that it can be manufactured using current integrated circuit (IC) fabrication technology enabling the integration of microelectronics with microsensors and microactuators [1]. MEMS technology has been used to successfully fabricate devices such as gyroscopes [1], pressure sensors [3], accelerometers [4], and many others [1]. This thesis focuses on the design, fabrication and characterization of MEMS relays using MetalMUMPS process, a commercial foundry process suitable for high volume manufacturing of MEMS relays.

In 1978 electrostatically actuated Microelectromechanical (MEMS) relays were first demonstrated by Petersen [5], [6]. Since then several MEMS relays and high-frequency MEMS switches have been developed by various researchers and are discussed in the literature [7], [8]. MEMS relays exhibit several advantages such as low loss, low power consumption, and absence of intermodulation distortion, compared to conventional semiconductor based switching devices. MEMS relays are preferable to other conventional semiconductor based switching devices such as field effect transistors, due to low loss, low power consumption, absence of intermodulation distortion and broad-band operation from DC to microwave frequency range [6]. Potential applications of MEMS relays include phased array antennas for radar systems, reconfigurable antennas,

Automatic Test Equipment (ATE) systems, industrial and medical instrumentation. MEMS relays would enable high performance system applications due to its potential for monolithic integration with electronics in a single chip. However, reliability of MEMS relays has been a major shortcoming that limits the use of MEMS in real world applications.

In recent years, reliability of MEMS relays have been studied by several research groups [9]-[19]. Reliability issues such as failure due to stiction and resistance degradation occurring over actuation cycles have been observed to be the key factors affecting the reliability of ohmic contact type MEMS relays. Stiction is unintentional sticking of movable and fixed parts in MEMS caused by surface forces leading to failure [20]. Failure due to stiction is frequently encountered in electrostatically actuated contact type MEMS relays. Typically, MEMS relays are designed for operation at low actuation voltages, which necessitates the design of movable micromechanical parts with low restoring spring forces. Permanent failure due to stiction occurs when the restoring spring force of the movable part is lower than the attractive forces generated at the contact surfaces of the MEMS relays. Another common reliability issue in ohmic contact type MEMS relays is the degradation of resistance over many actuation cycles. Specifically, the resistance of the MEMS relays gradually increases with actuation cycles and after several million actuation cycles the resistance increases to a very high value leading to an unacceptably high insertion loss.

In this thesis, the reliability of ohmic multi-contact MEMS relays actuated using comb-drive electrostatic actuators have been investigated. Specifically, resistance versus voltage characteristics, stiction caused by humidity, and resistance degradation over

actuation cycles has been studied. Packaging of the MEMS relay was carried out and is discussed. The measured resistance versus voltage curves has been compared with simulated results from elastic and elasto-plastic asperity-contact models.

Chapter 2 of this thesis starts with an overview of MEMS relays in general, and a description of the presented MEMS relay. Design and simulation of the MEMS relay are discussed. The MetalMUMPS process used for the fabrication of the MEMS relay is detailed.

In Chapter 3, the experimental characterization of the MEMS relay including experimental setup, resistance versus voltage characteristics, and reliability testing are presented. Reliability issues such as stiction failure and resistance degradation are discussed. Preliminary work on packaging of the MEMS relay is presented.

Chapter 4 introduces elastic and elasto-plastic modeling of the MEMS relay contact surfaces, as well as multi-scale models. The models are used to predict the resistance versus voltage characteristics of the MEMS relay.

The thesis is concluded in Chapter 5 with a summary of the design, modeling, fabrication, testing and packaging of the MEMS relay. Suggestions for improving the results obtained in this work are also discussed in this chapter.

CHAPTER 2 MEMS RELAY DESIGN

2.1 Introduction

In the past, vertically and laterally actuated MEMS relays have been developed. Various mechanical structural designs such as cantilevers [1], [6], [11], [21], [22], bridge structures [23], [15], [24], and others have been used for vertically actuated MEMS relays. Rotary actuators [25], cantilevers [27], comb-drive actuators [14], [28] have been used for implementation of lateral contact switches. Various actuation methods have been used for operation of MEMS relays including electromagnetic, electrostatic, piezoelectric and electro-thermal [21], [25]. Electrostatic actuation is most commonly employed in MEMS relays due to low power consumption.

The complete configuration of the proposed electrostatically actuated MEMS relay is shown in Figure 2-1. The MEMS relay has four main components, namely, the comb drive actuators (top and bottom), the folded suspension spring, the main beam, and the RF contacts. In the following sections, the configuration of the MEMS relay, the design of the comb drive and folded spring, and the fabrication of the MEMS relay are described.

2.2 MEMS Relay Configuration

The relay consists of a movable main beam anchored to the substrate using two identical folded suspension springs as shown in Figure 2-1(a). Comb-drive electrostatic actuators located at the top and bottom ends of the main beam enable bi-directional

actuation. RF ports (1 & 2) consist of five movable fingers connected to the movable main beam and six fixed fingers anchored to the substrate. The relay consists of two DC bias pads (A & B), four DC ground pads (G1, G2, G3 & G4) and two RF ports (RF port 1 & 2) as shown in Figure 2-1 (b). All the DC ground pads are electrically connected to one another through the main beam. Normally, in the open state, the movable fingers and the fixed fingers are separated by 8 μm. When the bottom-comb drive is actuated by applying a DC bias voltage between the DC bias pad B and a DC ground pad the main beam moves downwards and the movable fingers makes contact with the fixed fingers at the RF ports. Figure 2-1 (b) shows the closed state of the MEMS relay when the bottom comb-drive is actuated. Similarly, closed state could be obtained by actuating the top comb-drive.

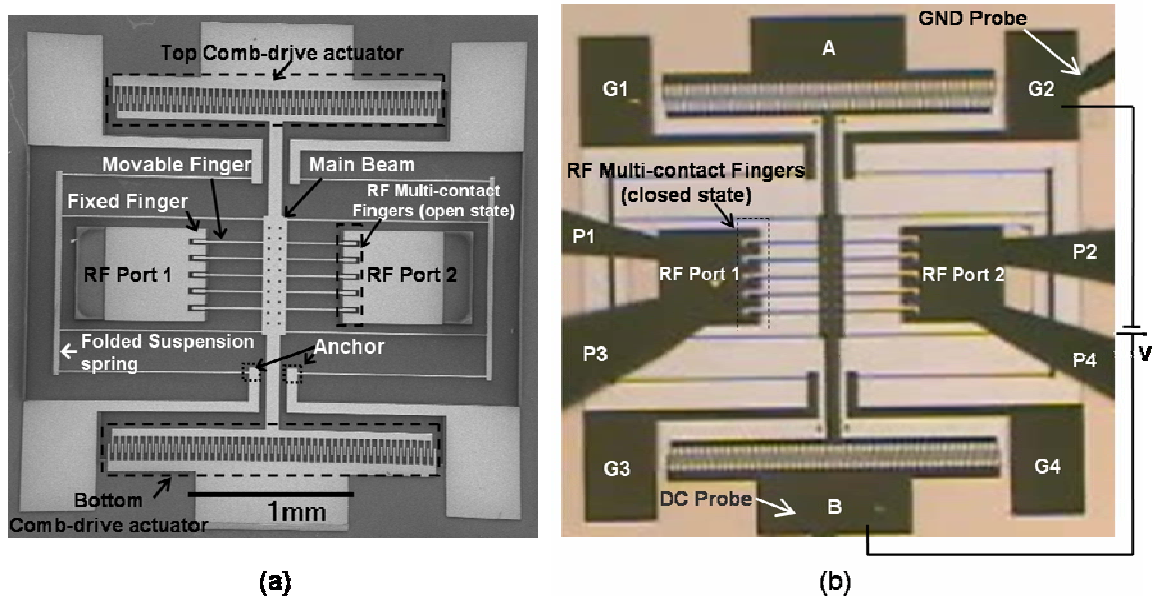

Figure 2-1 Multi-contact MEMS relay using comb-drive actuators (a) open state, and (b) closed state

The attractive features of this design include: a) the multi-contact design reduces stress at the contacts, b) the multi-contact design enables operation even in case of failure

of one or more of the contact fingers, and c) the bi-directional comb-drive design allows operation of the MEMS relays in case of poor contact or failure of one of the two contacting sides, and permits the ability to pull apart adhered contacts by actuating the comb-drive on the opposite side.

2.3 MEMS Relay Design

In this section, design of two of the MEMS relay components, namely the comb drive and the folded suspension spring elements are described.

2.3.1 Comb Drive Design

A comb drive is an electrostatic actuator (also known as interdigital actuator) that uses both electrostatic energy, from a DC voltage applied between the moving and fixed comb drive structures, and the mechanical restoring force provided by the spring structure [1]. The movement of comb drive actuators is constrained to only allow movement in the lateral y-direction (Figure 2-2).

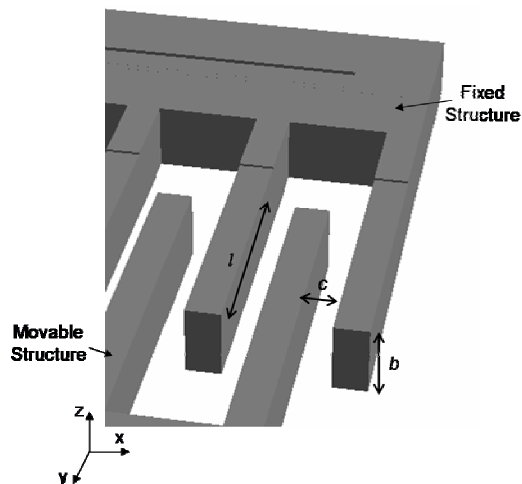

Figure 2-2 Comb drive actuator structure

The electrostatic energy stored in the comb drive actuator for a DC voltage V applied between the fixed and movable structures is given by [29]

$$U_E(y) = \frac{1}{2} C(y) V^2 \tag{1}$$

with

$$C(y) = \frac{n \varepsilon_0 \varepsilon_r l b}{c} \tag{2}$$

where *C(y)* is the capacitance between the fixed and movable structures of the comb drive, ignoring the capacity produced by the fringing fields; *n* is the number of gaps between comb drive fingers (equal to the total number of fingers minus one), ε_0 is the permittivity of free space, ε_r is the permittivity of the dielectric between fingers, *b* is the thickness of the nickel, and *c* is the width of the gap between fingers.

The voltage source supplies energy ($\delta U_b = V\delta Q$, $Q = CV$). This energy is the energy stored in the spring (mechanical work, $\delta W_M = F_E \delta y$) plus the energy that is stored at the electric field of the capacitor (δU_E)[1].

$$\delta U_b = \delta W_M + \delta U_E \tag{3}$$

The electrostatic force can be obtained as

$$F_E = \left. \frac{\delta U_b}{\delta y} \right|_{\delta y \to 0} - \left. \frac{\delta U_E}{\delta y} \right|_{\delta y \to 0} = \frac{dU_b}{dy} - \frac{dU_E}{dy} = \frac{1}{2} \frac{dC(y)}{dy} V^2 \tag{4}$$

Substituting Equation (2) in (3)

$$F_E = \frac{1}{2} \frac{n \varepsilon_0 \varepsilon_r b}{c} V^2 \tag{5}$$

A pair of comb drives were designed for the MEMS relay, to allow movement in the + and – y directions. From the MetalMUMPs design rules [30] the minimum allowable space between nickel structures is 8 μm. In this design, a value of 10 μm was

chosen for *c*. Other chosen design parameter values are shown in Table 2-1. The only variables in Equation (1) are *V*, and *n*. Equation (6) gives the restoring mechanical force.

$$F_M = kx \tag{6}$$

Where k is the spring constant, and x is the displacement of the movable comb structure. The displacement is the distance the MEMS relay must travel to make contact. For the MEMS relay design described in this thesis, the maximum displacement is the distance between the fixed and movable contacts, 8 μm. Equating Equations (5) and (6), we obtain an expression for *V* in terms of *n* and *k.*

$$V = \sqrt{\frac{2xck}{n\varepsilon_0\varepsilon_r b}} \tag{7}$$

2.3.2 Folded Suspension Spring Design

The folded suspension spring shown in Figure 2-3 was chosen because it avoids lateral instability during actuation.

Figure 2-3 Basic folded suspension spring design schematic.

In order to find the spring constant for the design shown in Figure 2-3 assume that each truss in the folded suspension spring is a cantilever beam of length *L*. The spring constant of a cantilever beam [31] with length *L/2* is

$$k_0 = \frac{2Ea^3b}{L^3} \tag{8}$$

Where E is the Young's Modulus of the beam material, a is the width of the beam, b is the thickness of the beam and L is the length of the truss.

First, half of the folded suspension spring design shown in Figure 2-3 is considered. Each truss is assumed to have a length of L and two k_0 spring constants in series. When springs are in parallel, the spring constants add so the equivalent spring constant is: $k_{eq} = k_1 + k_2 + k_3 + \ldots$. The equivalent spring constant for springs in series is $\frac{1}{k_{eq}} = \frac{1}{k_1} + \frac{1}{k_2} + \frac{1}{k_3} + \ldots$ [32]. The resulting spring constant for half of the folded suspension spring is $k_0/2$, as shown in Figure 2-4. The two halves of the folded suspension spring are in parallel, and therefore their spring constant add, so that the total spring constant for the MEMS relay is $k = k_0$ as shown in Equation (8).

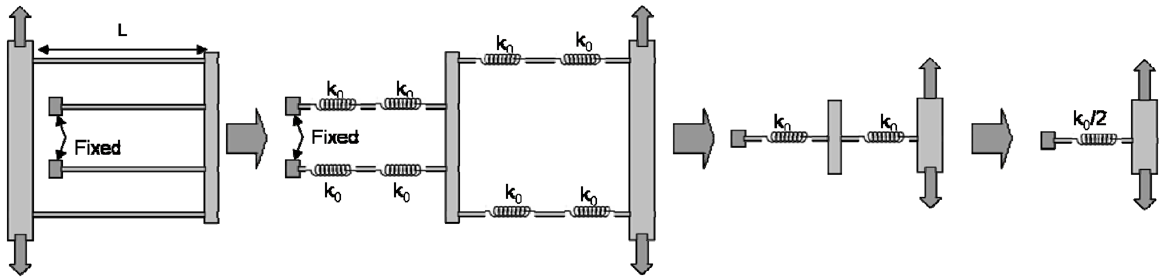

Figure 2-4 Schematic for folded suspension spring derivation

Substituting Equation (8) for k in Equation (7), the expression for actuation voltage can be written as

$$V = \sqrt{\frac{4xcEa^3}{n\varepsilon_0\varepsilon_r L^3}} = \sqrt{\frac{4.16\times10^{-3}}{nL^3}} \tag{9}$$

Various design parameters used in the MEMS relay design are shown in Table 2-1. In order to keep the overall size of the MEMS relay relatively small, optimal values for *L* and *n* were chosen to be 1140 μm and 98 respectively. The contact voltage for this optimal design is calculated to be 150 V.

Table 2-1 Design parameters for the comb drives and the folded springs.

Young's Modulus: E =1.8×10^5 MPa	Gap between comb fingers: c = 10 μm
Comb displacement: x = 8 μm	Permittivity of free space: $\varepsilon_0 = 8.854 \times 10^{-12}$ F/m
Width of spring beam: a = 8 μm	Permitivity of air: ε_r (air) = 1

2.4 MEMS Relay Simulation

Once the initial design of the MEMS relay was completed, CoventorWare™ [33] was used to perform electromechanical simulation of the relay. Considering the symmetry of the relay, only half of the nickel layer of the relay was meshed for simulation as shown in Figure 2-5. The mesh was created using Manhattan Bricks with linear element model with x, y and z element sizes of 10, 10 and 7 μm respectively.

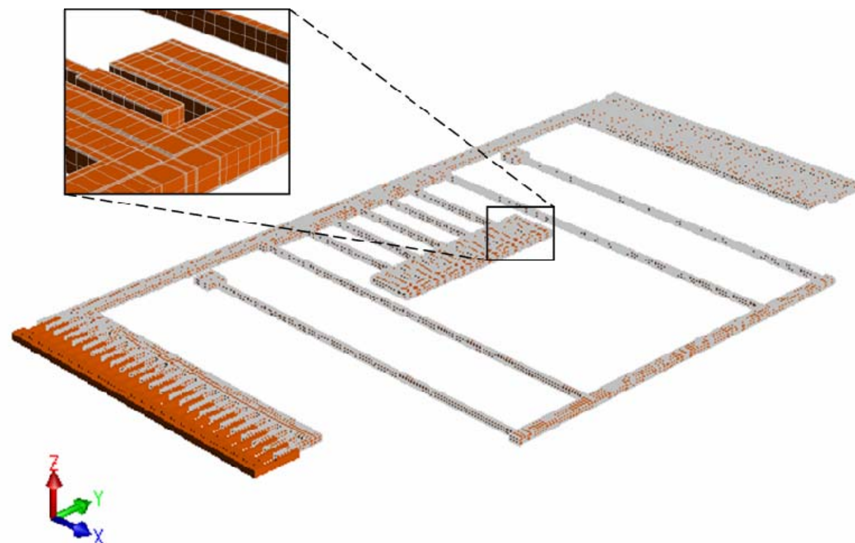

Figure 2-5 MEMS relay 3D meshed model of the MEMS relay used for simulation in Coventorware.

2.4.1 Boundary Conditions

Several boundary conditions (BCs) were set for simulation. Surface BCs include fixing movement in all directions at the bottom surface of the fixed comb-drive, the RF contact and spring anchors. Also, the side surface of the MEMS relay at the plane of symmetry (shown in Figure 2-6) was fixed in the x-direction and the bottom surface of the movable structure of the MEMS relay was fixed in the z-direction. Contact BCs were set only for one pair of RF fixed contact surface and movable MEMS relay contact surface, with an offset in the y-direction of 2 µm to account for the 1 µm platted gold at each surface that was not added to the mesh model. Simulation failed when contact BCs were applied to all contact surfaces.

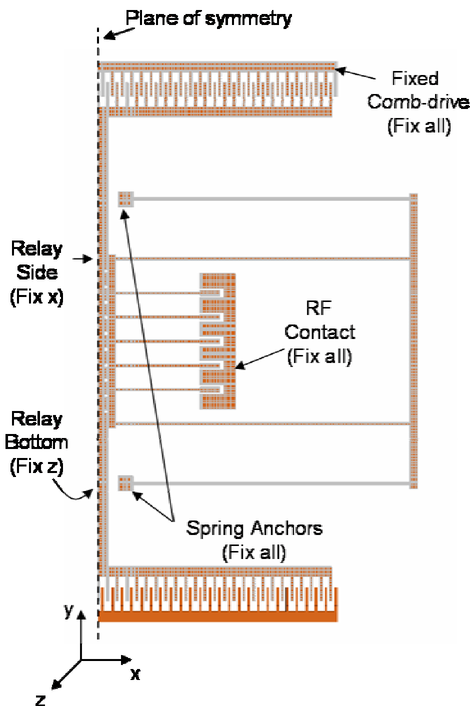

Figure 2-6 CoventorWare model of the MEMS relay showing various boundary conditions

2.4.2 CoSolve Results

CoSolve tool available in CoventorWare [33] was used to perform a coupled electro-mechanical simulation using the boundary conditions discussed earlier. Voltages were applied ranging from 70 V to 170 V. A trajectory analysis with a relaxation iteration method was used. The RF contact was not included in the simulation to decrease the simulation time. The results from both theoretical calculation (using equation (5)) and cosolve simulation are shown in Figure 2-7. It can be noted that the displacement from both theoretical and simulated results exhibit an increasing trend with the applied voltage. The theoretical calculation ignores the effect of fringing fields and therefore the calculated voltages are higher than that of the simulated values. It can be noted from the simulation results that the contact happens at 10 μm for a voltage of around 130 V.

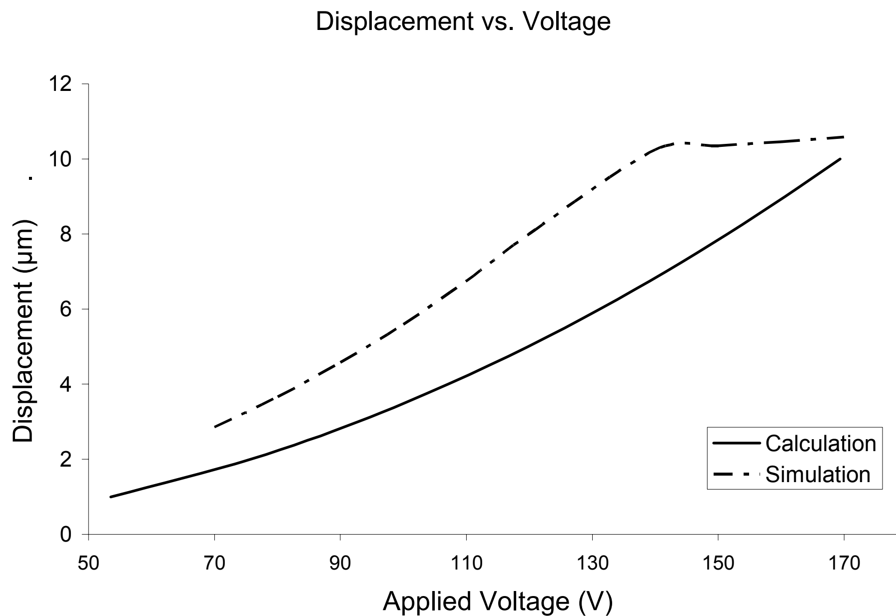

Figure 2-7 Displacement versus Applied Voltage characteristics for the MEMS relay.

2.5 MEMS Relay Fabrication

In this section, the fabrication of the MEMS relay will be discussed. The MEMS relay has been fabricated using the MetalMUMPs process (Run #8) available from MEMSCAP [30]. MetalMUMPs process is suitable for high volume manufacturing of MEMS relays. In the past, MetalMUMPs process has been used for fabrication of Poly/Nickel powered gripper [30], thermal actuator based bi-stable micro-relay [30], and MEMS variable capacitor [34].

2.5.1 MetalMUMPs Design Rules

The MetalMUMPs design handbook [30] provides two very important tables summarizing the design rules. Table 2-2 shows the minimum feature sizes and spacing for each layer and Table 2-3 shows the minimum enclosure and spacing between layers. For example, the features in the OXIDE1 mask must enclose the NITRHOLE mask features by five microns.

Table 2-2 Mask level names, minimum features and minimum space for each mask level in the MetalMUMPS process.

Mask Level Name	Minimum Feature (μm)	Minimum Space (μm)
OXIDE1	20	20
NITRHOLE	5	5
METANCH	50	10
METAL	8	8
GOLDOVP	50	50
HOLEM	8	8

Table 2-3 Design Rules between layers in the MetalMUMPS process.

Rule	Minimum Value (μm)
OXIDE1 enclose NITRHOLE	5.0
POLY enclose NITRHOLE	5.0
NITRHOLE space to POLY	5.0
METAL enclose NITRHOLE	25.0
METAL enclose METANCH	5.0
Lateral Etch Holes space in Nitride	≤ 100.0 (max. value)
Lateral Etch Holes space in Metal	≤ 100.0 (max. value)

2.5.2 MetalMUMPs Fabrication Process

MetalMUMPs process is an electroplated nickel surface micromachining process. MetalMUMPs process (shown in Figure 2) consists of a 20 μm thick electroplated nickel layer, 1-3 μm gold layer, two nitride layers (Nitride 1 & Nitride 2), a polysilicon layer (Poly), and an isolation oxide layer; all deposited on a silicon substrate (n-type <100> with 1-2 Ω-cm resistivity). The nickel layer is used as the structural layer for defining movable MEMS parts. The process allows formation of 25 μm deep trenches underneath the movable parts.

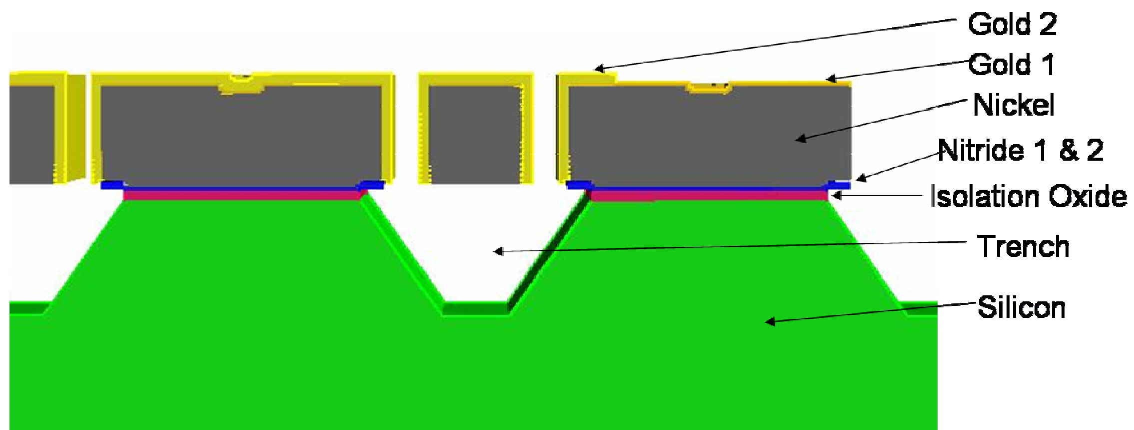

Figure 2-8 Cross section of MetalMUMPs process showing various layers.

2.5.2.1 Process Steps

The process steps involved in the fabrication of the MEMS relay using the MetalMUMPs Design Handbook [30] are described below.

Step 1: N-type <100> silicon wafer with 2 μm thick silicon dioxide isolation layer is used as the starting substrate for the MEMS relay. Figure 2-9 shows the top view and the cross section of the substrate.

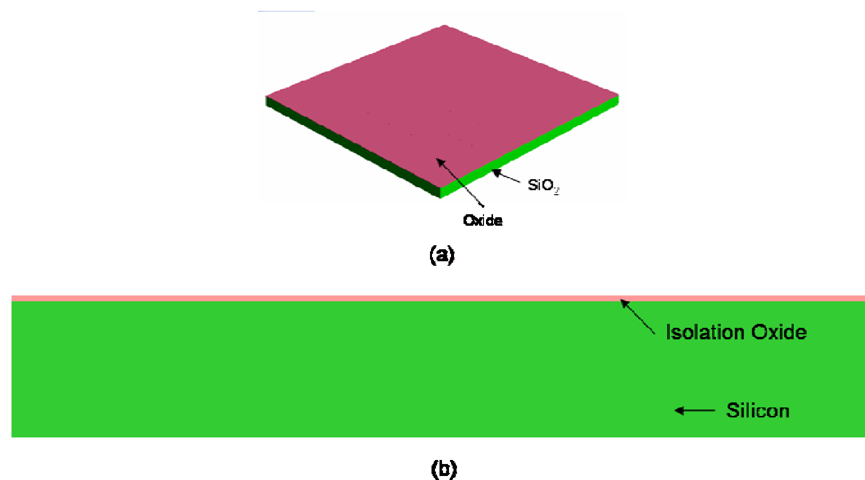

Figure 2-9 Step 1 in the fabrication of the MEMS relay using the MetalMUMPs process (a) top view, and (b) cross section.

Step 2: Oxide 1 layer is a 0.5 μm thick PSG layer that is used as a sacrificial release layer (shown in Figure 2-10 (a)). This layer is patterned by lithography using the OXIDE 1 mask shown in Figure 2-10(b) to define the silicon trench below the moving parts of the MEMS relay. The cross section of the patterned OXIDE 1 layer is shown in Figure 2-10(c).

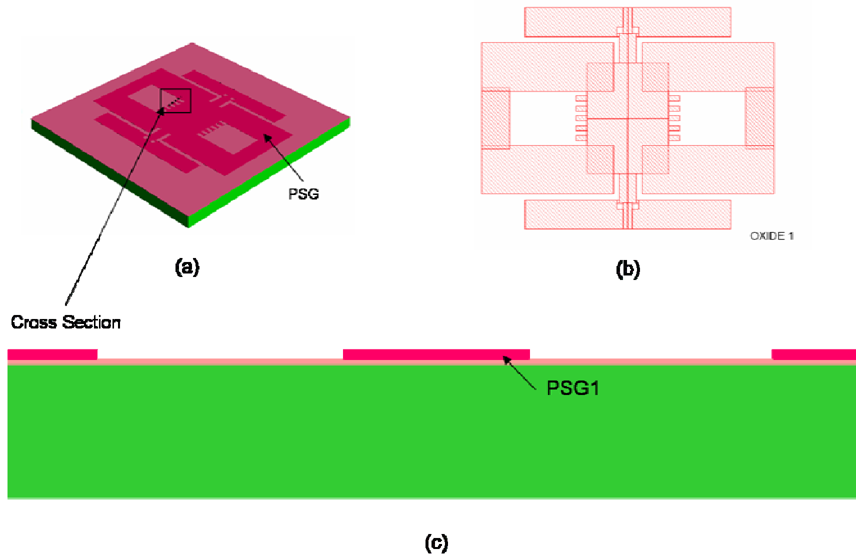

Figure 2-10 Step 2 in the MetalMUMPs process step 2 (a) top view, (b) OXIDE 1 mask layout, and (c) cross section of the oxide 1 layer.

Step 3: Two low stress silicon nitride layers of thickness 0.35 μm each are used for anchoring the fixed parts of the MEMS relay to the substrate and for defining the trenches in the substrate. The nitride is patterned using the NITRHOLE mask layer, where nitride is removed where the mask is dark as shown in Figure 2-11 (a) and (b). The cross section is shown in Figure 2-11 (c). The polysilicon layer (Poly) supported by the MetalMUMPs process is not used in this design.

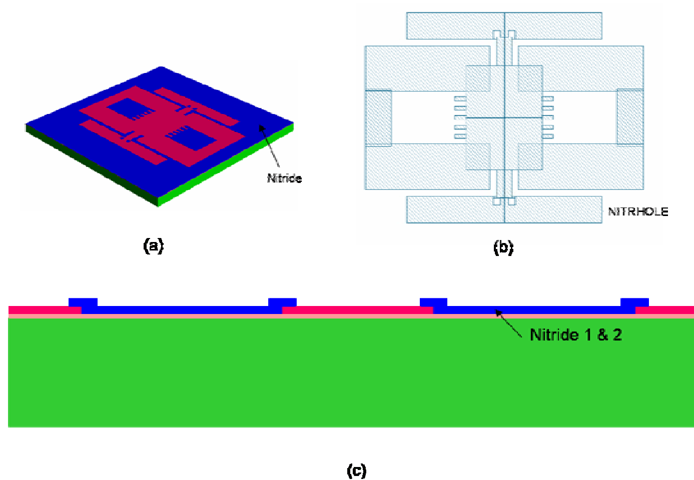

Figure 2-11 Step 3 in the MetalMUMPs process (a) top view, (b) NITRHOLE mask layout, and (c) cross section of the nitride layer.

Step 4: The Oxide 2 layer (1.1 μm thick PSG), is deposited where the moving parts of the Metal (Nickel) layer will be released. The top view of the MEMS relay at this step is shown in Figure 2-12(a). The METANCH mask layer shown in Figure 2-12(b) is used to define the Oxide 2 layer. PSG should not be present at the anchoring locations. The cross section of the MEMS relay at this step is shown in Figure 2-12(c).

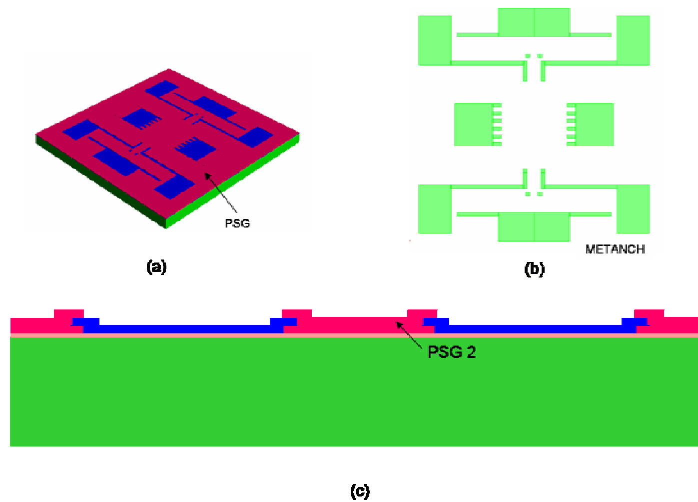

Figure 2-12 Step 4 in the MetalMUMPs process (a) top view, (b) METANCH mask layout, and (c) cross section of the oxide 2 layer.

Step 5: Thin layers of Cr (10 nm) and Pt (25 nm) are deposited at the Anchor locations as shown in Figure 2-13 (a). The METANCH mask shown in Figure 2-13 (b) is also used to define the Cr and Pt layer. Thick layers of Cu (500 nm) and Ti (50 nm) are deposited to form the plating base (not shown) for the Nickel. The cross section for this step not including the Cu and Ti layer is shown in Figure 2-13(c).

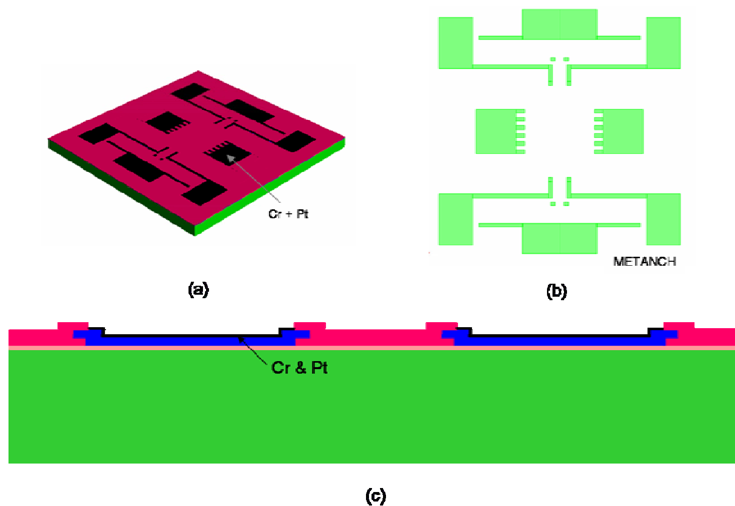

Figure 2-13 Step 5 in the MetalMUMPs process (a) top view, (b) METANCH mask layout, and (c) cross section of the metal layer.

Step 6: Thick photoresist is deposited to form the stencil for electro-plating the nickel structure. The METAL mask shown in Figure 2-13(b) is used to define the photoresist stencil. The HOLEM mask level (not shown) is included in the METAL mask to define the etch holes to improve the release process. The cross section of this step is shown in Figure 2-14.

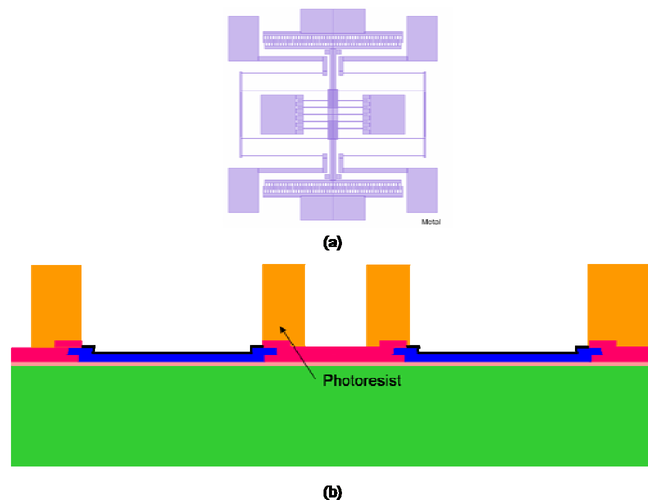

Figure 2-14 Step 6 in the MetalMUMPs process , (a) METAL mask layout, and (b) cross section of the metal layer

Step 7: On top of the copper seed layer, a 20 μm thick Nickel is electroplated to form the structural layer of the MEMS relay. A 0.5 μm gold layer is plated on top of the Nickel. Figure 2-15 (a) shows the top view of the MEMS relay without the thick photoresist, and Figure 2-15(b) shows the cross section of the MEMS relay.

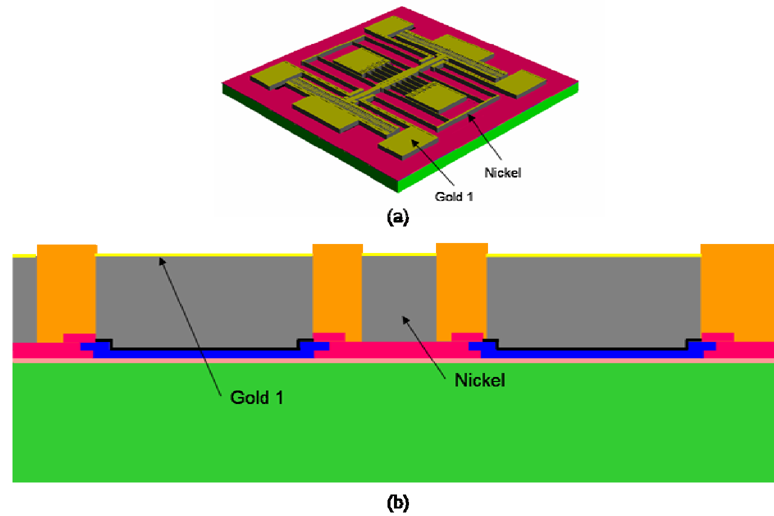

Figure 2-15 Step 7 in the MetalMUMPs process (a) top view, and (b) cross section of the contacts.

Step 8: The thick photoresist is removed at the contact areas only. A new photoresist layer is applied to protect the top of the MEMS relay, and a 2 μm thick gold layer is electroplated only at the top and sidewalls of the RF contacts. The mask used in this step is shown in Figure 2-16(b). The top view without the photoresist is shown in Figure 2-16(a) and the cross section of this step is shown in Figure 2-16(c).

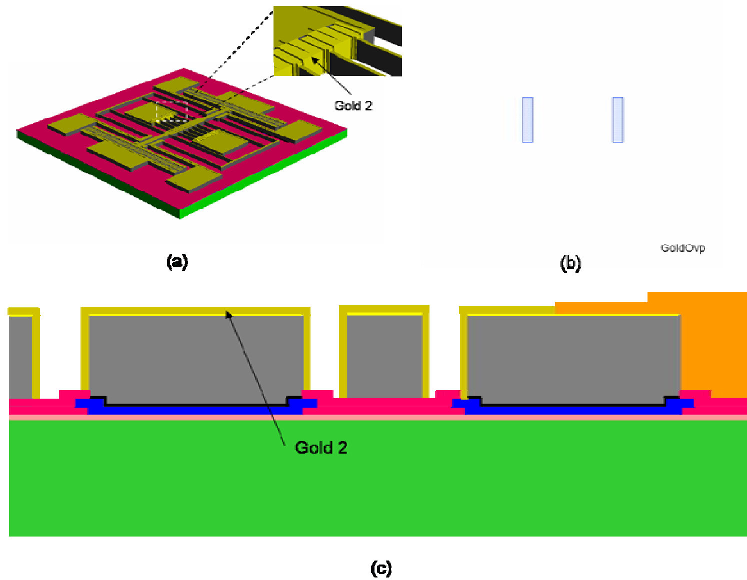

Figure 2-16 Step 8 in the MetalMUMPs process (a) top view, (b) GOLDOVP mask layout, and (c) cross section.

Step 9: The photoresist is removed and wet chemical etches are used to release the plating base and the isolation oxide layer over the area where the trenches will be formed. KOH is used to create the Silicon trenches to form the MEMS relay. The completed top view and cross section of the MEMS relay is shown in Figure 2-17.

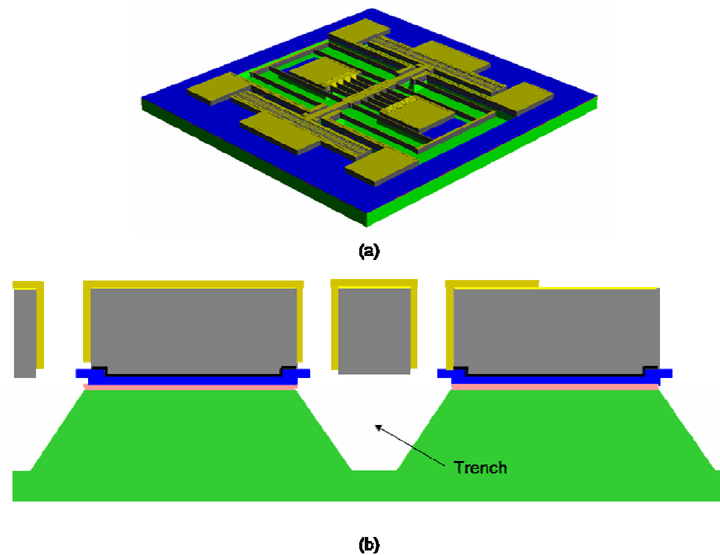

Figure 2-17 Step 9 in the MetalMUMPs process (a) top view, and (b) cross section.

In this chapter, configuration, design, simulation, and fabrication of the MEMS relay were discussed. In the next chapter, resistance versus voltage characteristics, reliability, and packaging of the MEMS relay are discussed.

CHAPTER 3 EXPERIMENTAL CHARACTERIZATION

In the previous chapter, the MEMS relay design was explained along with its fabrication process. In this chapter, the resistance versus voltage characteristics of the MEMS relay is described. Also reliability issues such as stiction caused by humidity, resistance degradation over actuation cycles, and packaging are discussed.

3.1 Experimental Setup

The experimental setup used for testing MEMS relays is shown in Figure 3-1. The setup consists of an Agilent 33220A function generator, Krohnit 7600 Wideband Amplifier, HP 54501A Oscilloscope, MM8060 Micromanipulator probe station, and HP3468A 4-wire Multimeter. The MEMS relay operation is monitored using a CRT display interfaced to the microscope through a CCD camera. The output of the function generator is set to a 5 V 10 Hz square wave with a 50% duty cycle. The output of the function generator is input to the amplifier and the output of the amplifier is connected to the DC and ground probes in the probe station. The output of the amplifier is measured using a low voltage oscilloscope through a ten times probe to reduce the amplifier output voltage by a factor of 10. The resistance of the MEMS relay is measured using the 4-wire multimeter. The two current source wires are connected to probes P1 and P2 and the two voltage sensing wires are connected to probes P3 and P4.

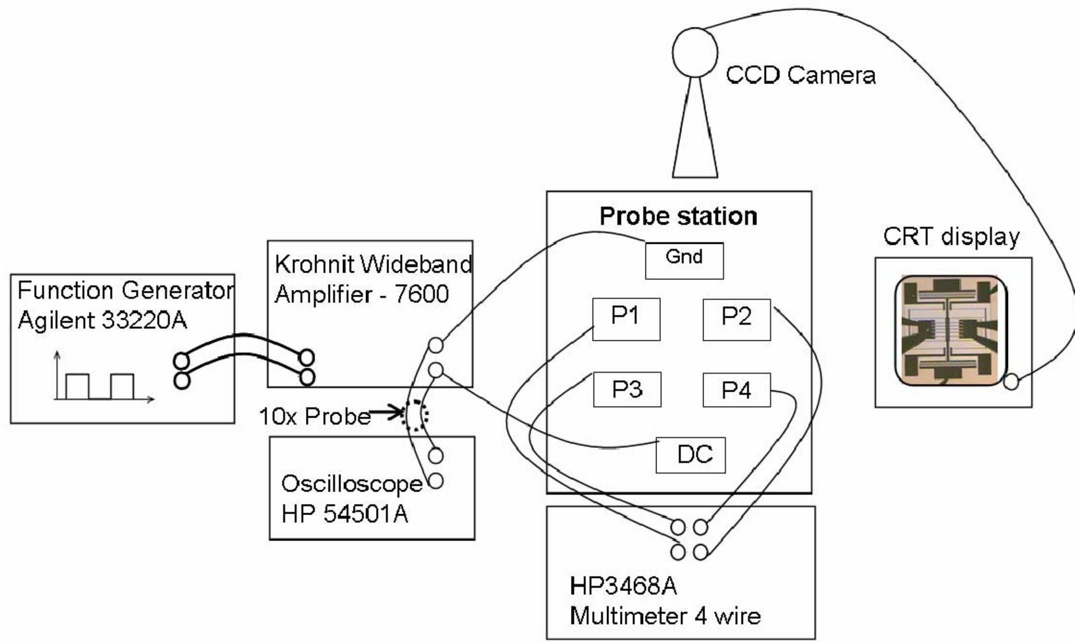

(a)

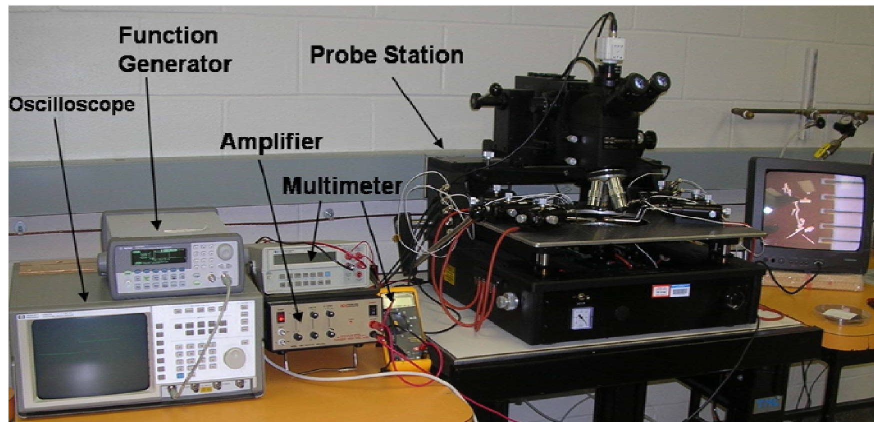

(b)

Figure 3-1 Experimental setup for testing the MEMS relay (a) Schematic Block diagram, (b) photograph of the setup.

3.2 Resistance vs. Voltage Characteristics

The resistance versus voltage characteristics of the MEMS relays has been measured using the experimental setup discussed above. Initially, the MEMS relay was actuated for approximately 5,000 cycles using a 10 Hz square wave signal and then the

resistance versus voltage characteristics has been measured. A DC bias voltage is applied between the fixed part of the comb-drive and the movable main beam of the MEMS relay through the DC probe and the ground, respectively. It was observed that the movable fingers make contact with the fixed fingers at 120 V but the contact remains open up to 171 V. At 172 V, the movable interdigital fingers establish connection with the fixed fingers and provide electrical continuity between RF ports 1 and 2. The resistance versus applied voltage characteristics of the MEMS relay has been measured several times in the range of 172 V to 220 V and the results are shown in Figure 5. The total resistance value between the RF ports 1 and 2 is in the range of 1.575 Ω to 0.451 Ω at 172 V. The resistance values decrease from an average value of 0.87 Ω to 0.31 Ω as the voltage is increased from 172 V to 188 V and thus exhibits a steep slope. The resistance values do not vary significantly in the range of 188 V to 220 V and gradually decreases to 0.23 ± 0.03 Ω at 220 V.

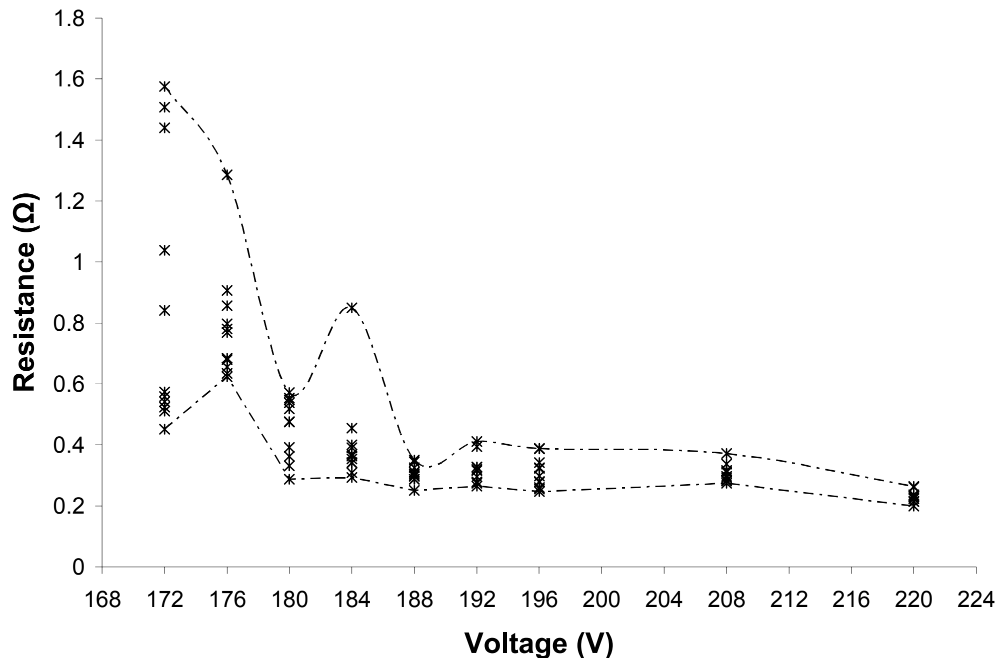

Figure 3-2 Measured resistance versus applied voltage characteristics of the MEMS relay

3.2.1 Resistance versus Applied Voltage for Other Contact Geometries

The MEMS relay design with planar contacting surfaces described so far in this thesis is referred as Type A Contact. In this section, the resistance versus voltage characteristics for MEMS relays with three other contact geometries (shown in Figure 3-3) are discussed. The measured 'resistance versus applied voltage' characteristics for all four contact geometries are shown in Figure 3-4. Contact geometry *A* has the lowest resistance, geometries *C* and *D* have comparable trends between 200 V and 220 V. Geometry *E* has the highest average resistance of all four geometries. Contact *C* and *E* remained open up to 184 V; whereas contact *A* and *D* were open up to 172V. This is probably because the contact areas of *A* and *D* are initially larger than the contact areas of *C* and *E*. Overall, resistance values of all four geometries exhibit a decreasing trend with increase in applied voltage.

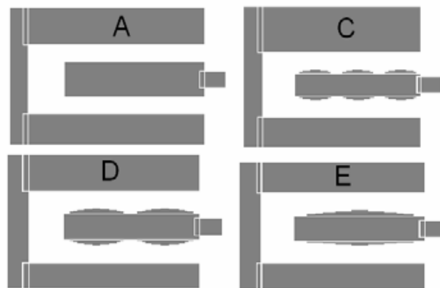

Figure 3-3 MEMS relays contact geometries

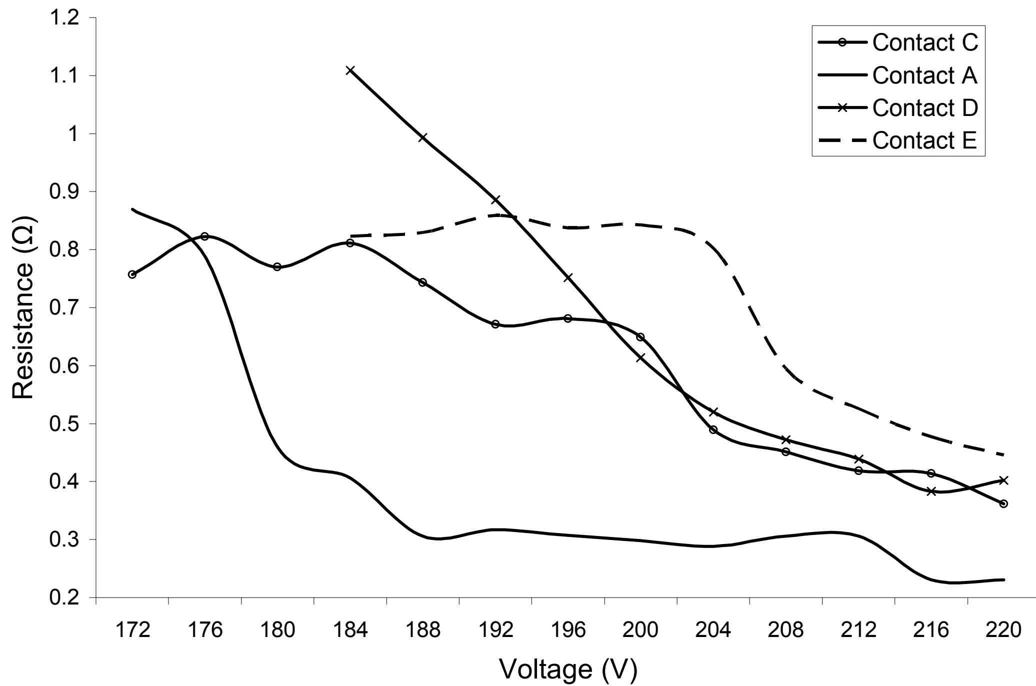

Figure 3-4 Comparison of average measured resistance versus applied voltage characteristics for MEMS relays with four different contact geometries as shown in Figure 3-3

3.3 Reliability Study

In this section, reliability issues such as stiction caused by humidity and resistance degradation over actuation cycles are discussed for MEMS relay with *Type A* contact design.

3.3.1 Stiction

A few MEMS relay chips from MetalMUMPs Run #8 were stored in normal environmental conditions for approximately three months inside a lab, where the devices are prone to absorb humidity. Typical humidity level was about 58% during this period. After three months, several MEMS relays were tested and stiction of the movable fingers to the fixed fingers occurred (as shown in Figure 3-5) after a few actuation cycles. In

order to verify whether humidity was the main cause of stiction, dehydration experiments were conducted at a temperature of 120°C for three hours. After the dehydration process, the relays were tested and stiction was not observed for several thousand actuation cycles. Resistance versus voltage characteristics of an example MEMS relay before and after dehydration process are shown in Figure 3-6. Overall, a similar trend was observed for resistance versus voltage curves before and after dehydration process.

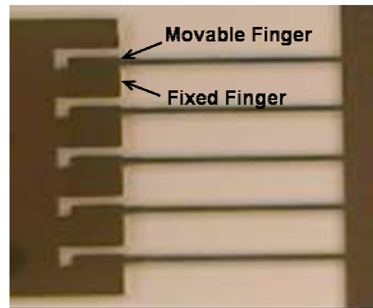

Figure 3-5 Stiction of the movable finger to the fixed fingers in the MEMS relay with Type A contact design.

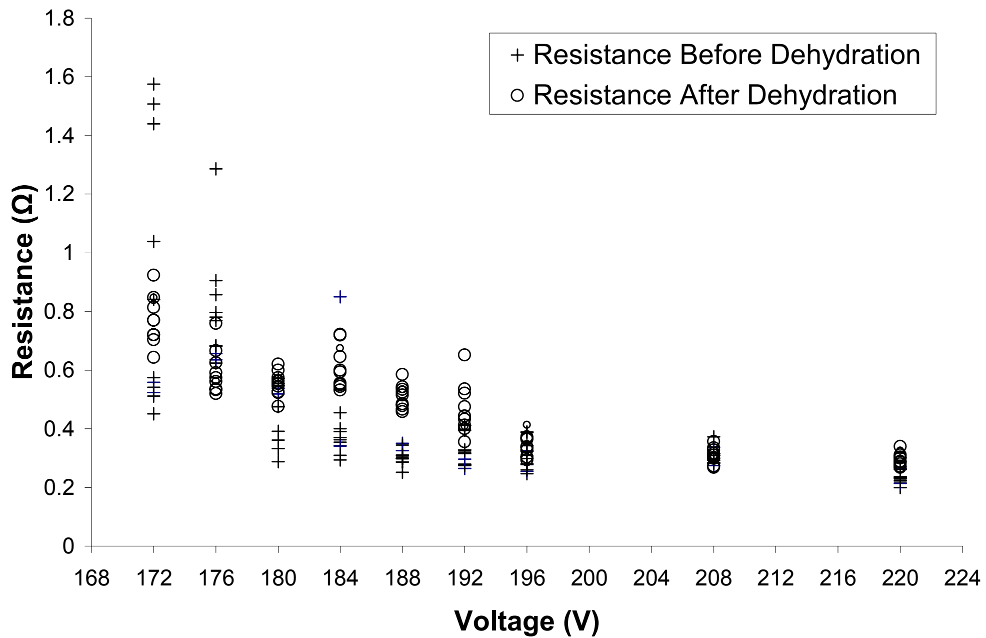

Figure 3-6 Resistance versus applied voltage characteristics before and after dehydration for MEMS relay with Type A contact design.

3.3.2 Lifetime Testing

The resistance value degradation of the relay over many actuation cycles was tested using a 10 Hz square wave and the results are shown in Figure 3-7. Initially, the contact surfaces are fairly rough and so the contact resistance would be limited to the asperity peaks. Therefore, initially the contact resistance was high. As the switch is operated, the asperity peaks wear out and lead to smoother contact surfaces, resulting in a decrease in the electrical contact resistance up to approximately 10^3 actuation cycles. Eventually, the surfaces reach a steady, stable range where the asperities are not wearing significantly, thus the contact resistance is nearly constant between 10^3 and 10^4 actuation cycles. Finally, the relay reaches a third phase of severe wear, which in theory could be attributed to micro-welding, fretting and surface fatigue. Two potential factors involved in micro-welding are gold-to-gold adhesion [35]-[37] and localized high current density at the asperity contact peaks. The difference in the resistance values between the top comb-drive and bottom comb-drive actuation cases could be attributed to the non-uniformity in the surface roughness profiles of the gold contact surfaces on the top and bottom sidewalls of the contact fingers. Overall both sides of the fingers exhibit similar resistance degradation trends. It can be noted that the bi-lateral actuation design doubles the lifetime of the relay. SEM pictures of the RF contact surface at the start of the reliability test and after $8x10^5$ actuation cycles are shown in Figure 3-8. It can be noted that the side wall contact surface at $8x10^5$ actuation cycles has considerably worn out when compared to the surface condition at the start of the test.

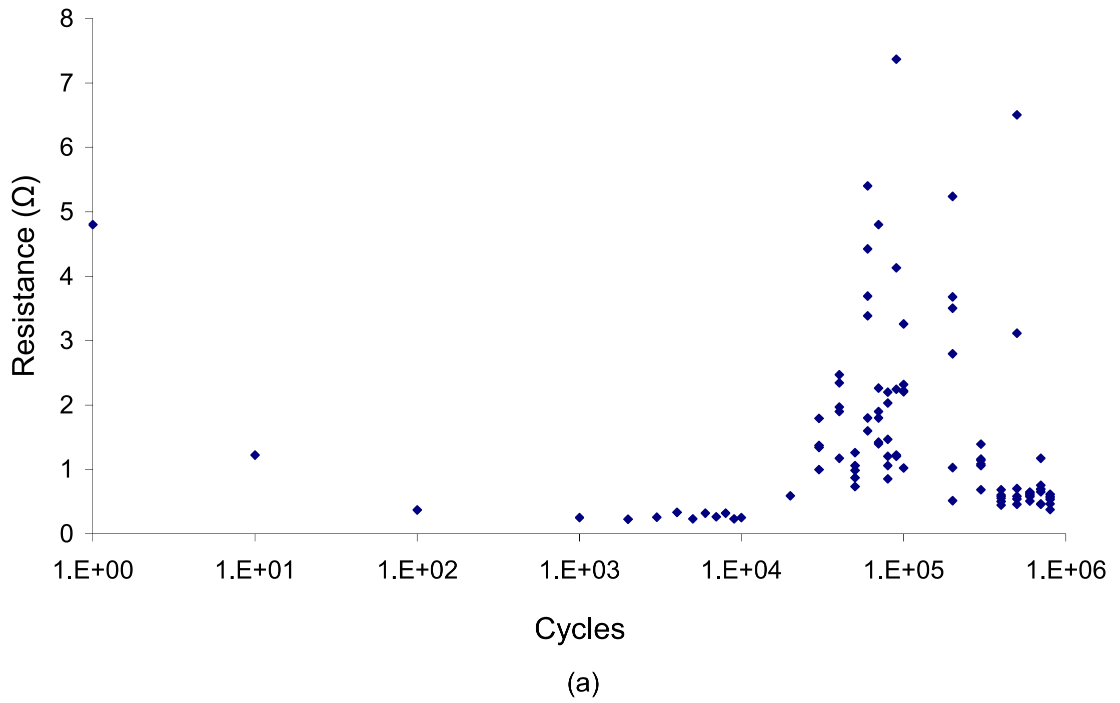

(a)

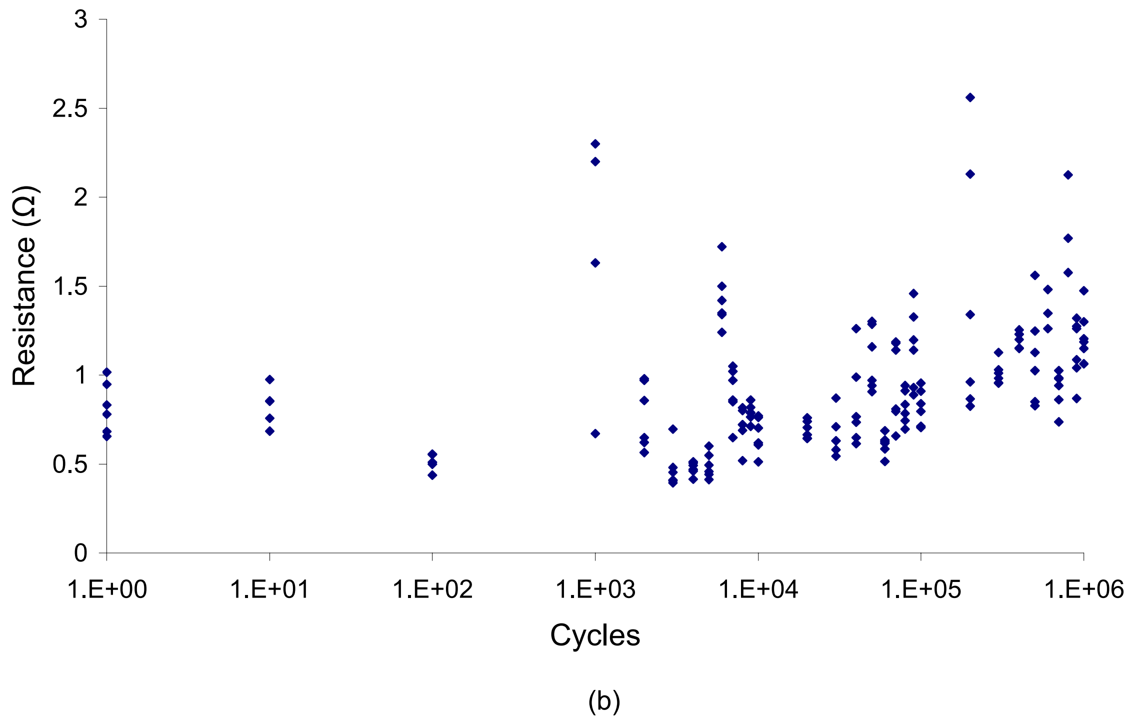

(b)

Figure 3-7 MEMS relay resistance degradation over actuation cycles for actuation voltage applied to (a) the top comb-drive actuator, and (b) bottom comb-drive actuator.

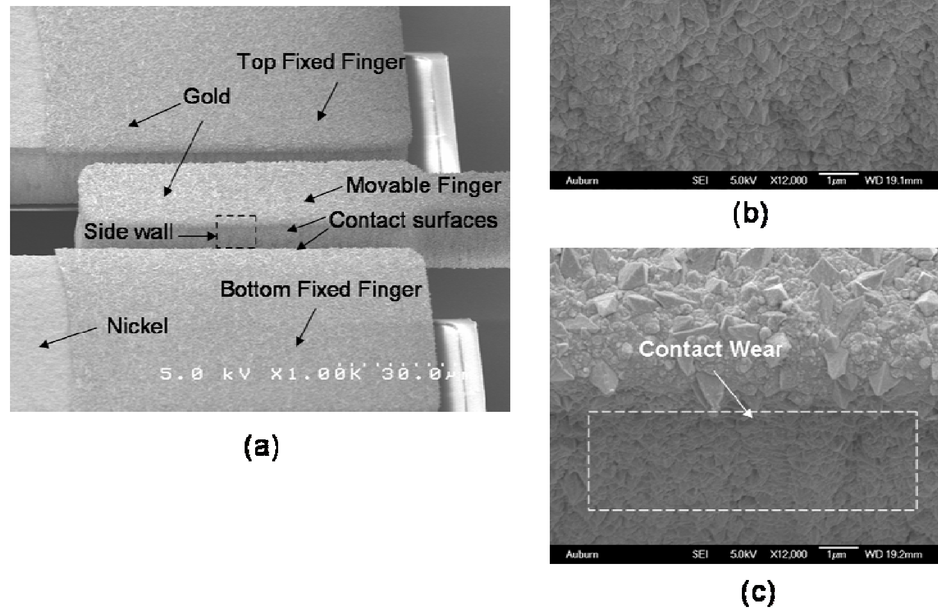

Figure 3-8 SEM picture of the RF contact in the MEMS relay (a) a movable finger located between the top and bottom fixed fingers in the open state, (b) side wall of the RF contact surface at the start of the reliability test, and (c) side wall of the RF contact surface after $8x10^5$ actuation cycles.

3.3.3 Reliability Test of Contact Geometry E

A second MEMS relay with contact geometry *E* as explained in section 3.3.1 was tested for reliability. The results are shown in Figure 3-9. After 300,000 cycles, the MEMS relay started to fail; a few of the measured resistances were opens. At 700,000 cycles this device failed completely, all the resistances measured were open even though mechanically the device continued to work properly. In this preliminary test, it was observed that MEMS relay with Type E contact exhibit poor reliability when compared to the MEMS relay with Type A contact.

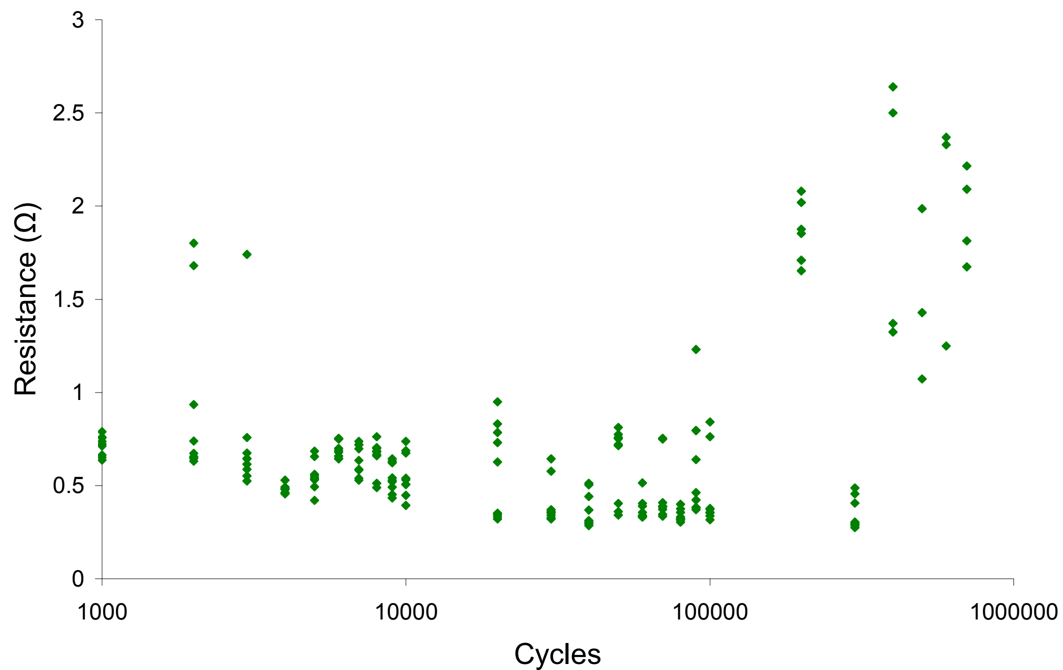

Figure 3-9 Resistance degradation over actuation cycles for the MEMS relay with Type E contact design

3.4 MEMS Relay Packaging

MEMS packaging requires special considerations depending on the application. For example, pressure sensor and humidity sensor must interact with the environment. Some issues in MEMS packaging include die handling and attach, outgassing, and stress [38]. In certain applications, packaging of MEMS is considered to be a major barrier in commercialization. Cost of packaging MEMS devices can consist of up to 95% of total production costs [39]. In this section, the packaging of the MEMS relay is presented. The MEMS relay does not need to interact with the environment. The main purposes of packaging include isolation of the MEMS relay from environmental factors such as humidity and particles. Further packaging facilitates interfacing of the MEMS relay with other electronics.

3.4.1 Package Selection

The packaging of the MEMS relay was accomplished using the facilities available at the Center for Advanced Vehicle Electronics (CAVE) at Auburn University. The package and lid used to package the MEMS relay was chosen with the help of Dr. Robert Dean from Auburn University. In this work, the package and lid part number shown in Table 3-1 were used.

Table 3-1 Part number and description of package and lid purchased from Spectrum Semiconductor Materials, Inc (www.spectrum-semi.com).

SSM P/N	DESCRIPTION
CPG06869	068 PGA Mfg Dwg: IPK68F1-8239A Cav: .440 x .440 D/A Plating: AU
CLG68001	COMBO LID Mfg Dwg: C-2716-3-50M-100MNI-GKL OD: .680 x .680 ID: .570 x .570

The chip to be packaged contains nine MEMS relays, and each one has seven connections to be wire bonded to the package. Therefore, the package should have more than 63 pins. The chosen package has 68 pins. The top pad layout, bottom pin layout and connection table are shown in Figure 3-10. A clear lid was chosen so that the relay movement can be observed even after the chip was packaged. The lid has a circular clear opening as shown in Figure 3-11.

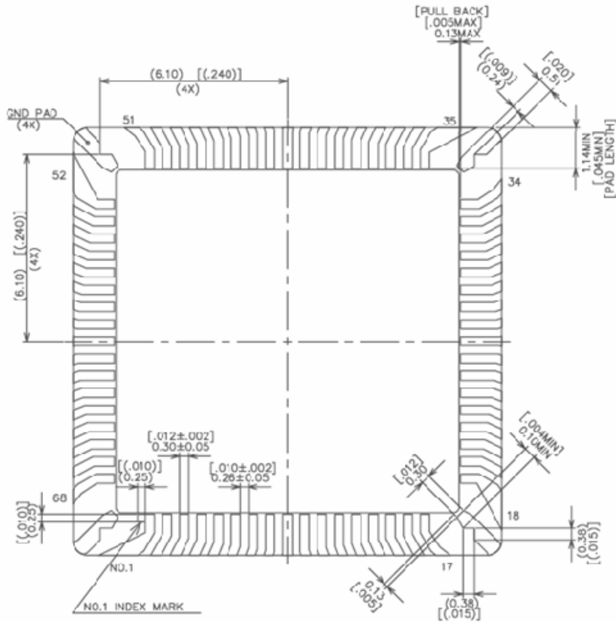

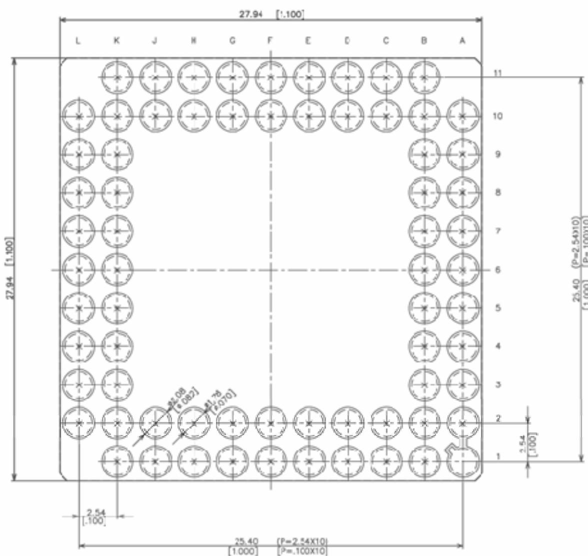

PAD	PIN	PAD	PIN	PAD	PIN
1	B2	26	K6	51	B11
2	B1	27	L6	52	B10
3	C2	28	K7	53	A10
4	C1	29	L7	54	B9
5	D2	30	K8	55	A9
6	D1	31	L8	56	B8
7	E2	32	K9	57	A8
8	E1	33	L9	58	B7
9	F2	34	L10	59	A7
10	F1	35	K10	60	B6
11	G2	36	K11	61	A6
12	G1	37	J10	62	B5
13	H2	38	J11	63	A5
14	H1	39	H10	64	B4
15	J2	40	H11	65	A4
16	J1	41	G10	66	B3
17	K1	42	G11	67	A3
18	K2	43	F10	68	A2
19	L2	44	F11		
20	K3	45	E10		
21	L3	46	E11		
22	K4	47	D10		
23	L4	48	D11		
24	K5	49	C10		
25	L5	50	C11		

(c)

Figure 3-10 Package details from the specification sheet provided by Spectrum Semiconductor Materials (a) top view, pad layout, (b) bottom view, pin layout, and (c) connection table.

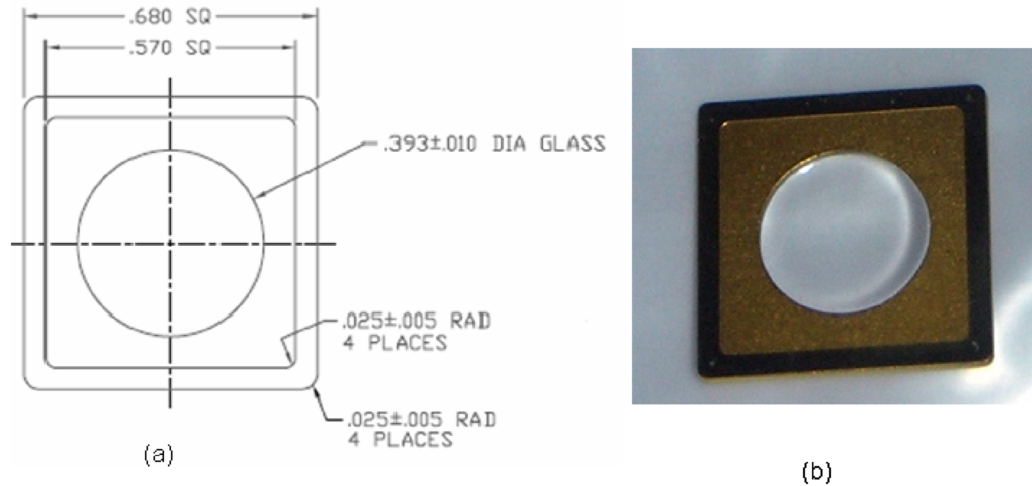

Figure 3-11 Chosen lid for packaging the MEMS relay (a) schematic, and (b) lid photograph

3.4.2 Wire Bond Arrangement

The chip containing the MEMS relays does not have any labels, therefore a schematic drawing was used to identify the pads on the chip and designate them to specific pads in the package. The schematic was also very useful in choosing the chip pad and package pad combinations. In order to relate specific pads on the chip with the corresponding pin number, each wire bonding location on the chip was labeled as shown in Figure 3-12(a). The schematic used for wire bonding is shown in Figure 3-12 (b). The corresponding pad and pin on the package for a specific relay pad can be found by consulting Table 3-2.

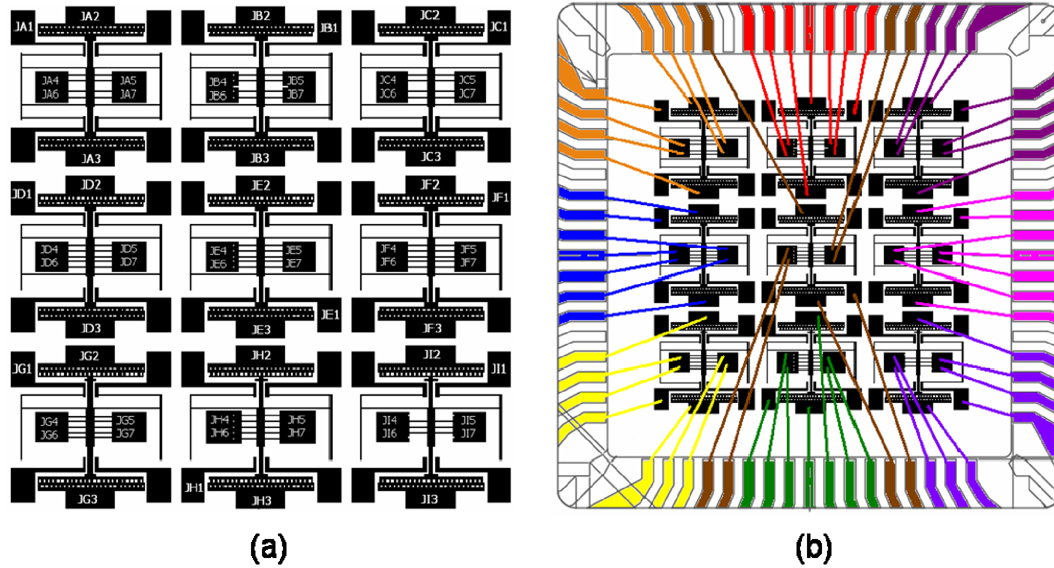

Figure 3-12 Chip schematic containing nine MEMS relays (a) chip pad labels, and (b) wire bonding schematic.

Table 3-2 Relationship between chip pad, package pad, and package pin.

Chip	PAD	PIN	Chip	PAD	PIN	Chip	PAD	PIN	Chip	PAD	PIN	Chip	PAD	PIN
JA1	1	B2	JC1	51	B11	JE1	65	A4	JG1	15	J2	JI1	37	J10
JA2	68	A2	JC2	52	B10	JE2	31	L8	JG2	14	H1	JI2	38	J11
JA3	4	C1	JC3	48	D11	JE3	30	K8	JG3	18	K1	JI3	34	L10
JA4	2	B1	JC4	54	B9	JE4	21	L3	JG4	16	J1	JI4	33	L9
JA5	66	B3	JC5	50	C11	JE5	56	B8	JG5	19	L2	JI5	36	K11
JA6	3	C2	JC6	53	A10	JE6	22	K4	JG6	17	K2	JI6	32	K9
JA7	67	A3	JC7	49	C10	JE7	55	A9	JG7	20	K3	JI7	35	K10
JB1	57	A8	JD1	7	E2	JF1	46	E11	JH1	23	L4			
JB2	60	B6	JD2	6	D1	JF2	45	E10	JH2	27	L6			
JB3	61	A6	JD3	12	g1	JF3	40	H11	JH3	26	K6			
JB4	62	B5	JD4	9	F2	JF4	44	F11	JH4	24	K5			
JB5	59	A7	JD5	8	E1	JF5	43	F10	JH5	29	L7			
JB6	63	A5	JD6	10	F1	JF6	41	G10	JH6	25	L5			
JB7	58	B7	JD7	11	G2	JF7	42	G11	JH7	28	K7			

3.4.3 Printed Circuit Board

For testing of the packaged MEMS relay, a printed circuit board (PCB) shown in Figure 3-13 (a) was developed with the assistance of Dr. Robert Dean, as shown in

Figure 3-13 (a). The PCB was fabricated by Advanced Circuits (www.4pcb.com/). A device socket for the package shown in Figure 3-13 (b) was purchased from Mill-Max (www.mill-max.com/ part # 510-93-068-11-061001) and soldered to the PCB as shown in Figure 3-13 (c) so that the packaged relay can be easily removed and replaced from the socket during testing. The PCB pads have the same labels as the corresponding package pin labels.

(a) (b) (c)

Figure 3-13 Printed circuit board for testing the packaged MEMS relay (a)Printed circuit board top view, (b) socket for the packaged relay, and (c) PCB along with the socket

3.4.4 Packaging Details

The wire bonding of the MEMS relay to the package was done using a Palomar 2460-IV wire bonding machine. The Palomar 2460-IV settings used is provided in Table 3-3.

Table 3-3 Palomar 2460-IV settings for wire bonding of MEMS relay chip

PROGRAM	12805:00	AUX	LOOP
50	80	125	2
50	85	110	10
50	85	200	60
I	I	0	60
25	25	10	**45**
10	10		
100	100		

After wire bonding, the lid was added to the package under vacuum. The instructions for sealing the lid provided by the manufacturer is given below:

1. Clips should have sufficient pressure to hold the lid in place. High clip pressure or pressure applied at the center of the lid only is not recommended. Clips should be designed to distribute pressure evenly to prevent oil-canning. A pressure spreader (nickel plated lids, ceramic or glass squares) can be used on larger lids to better distribute pressure evenly.
2. Furnace atmosphere can be nitrogen, hydrogen or hydrogen/nitrogen mixtures (forming gas). The usual atmosphere used is pure nitrogen with less than 10 ppm combined O_2 and H_2O.
3. The profile of a furnace should always be determined under load. The thermocouple leads should be placed in a package not on the belt. Please note that there are many acceptable profiles. Any profile that has the following basics is acceptable:
   - Rise time 35 to 50° C/min.
   - Time over 280°C should be a minimum of four (4) minutes.
   - Peak temperature of 320 to 350°C should be maintained for one to one and one-half minutes.

- Temperature drop of 35 to 50°C/min.

The packaged MEMS relay chip before and after placement of the lid are shown in Figure 3-14. The placement of the lid under vacuum was performed using an SST International 3150 high vacuum furnace. The lid placement settings used are shown in Figure 3-15. Some preliminary measurements were performed and future work is discussed in Chapter 5.

In this chapter, MEMS relay characteristics such as resistance versus voltage characteristics for MEMS relays with four different contact geometries and reliability have been discussed. Also some initial work on packaging of the relay was reported. In the next chapter, the electrical contact resistance (ECR) modeling of the MEMS relay is reported.

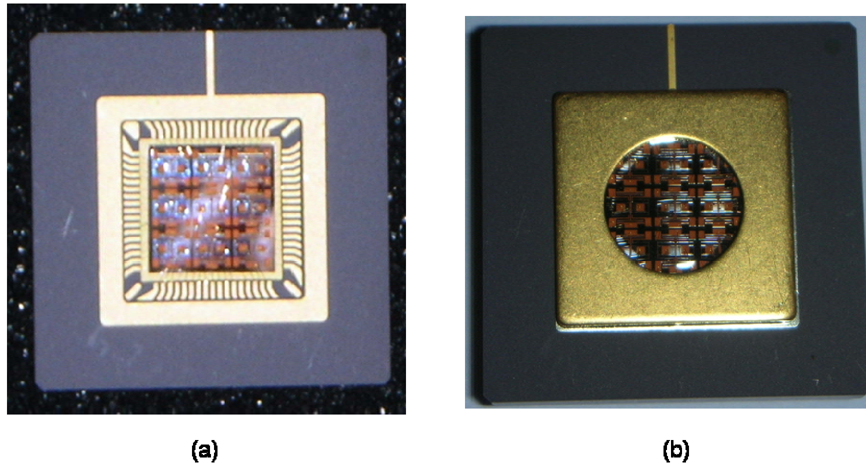

Figure 3-14 Package containing wire bonded MEMS relay (a) before glass lid sealing (b) after glass lid sealing.

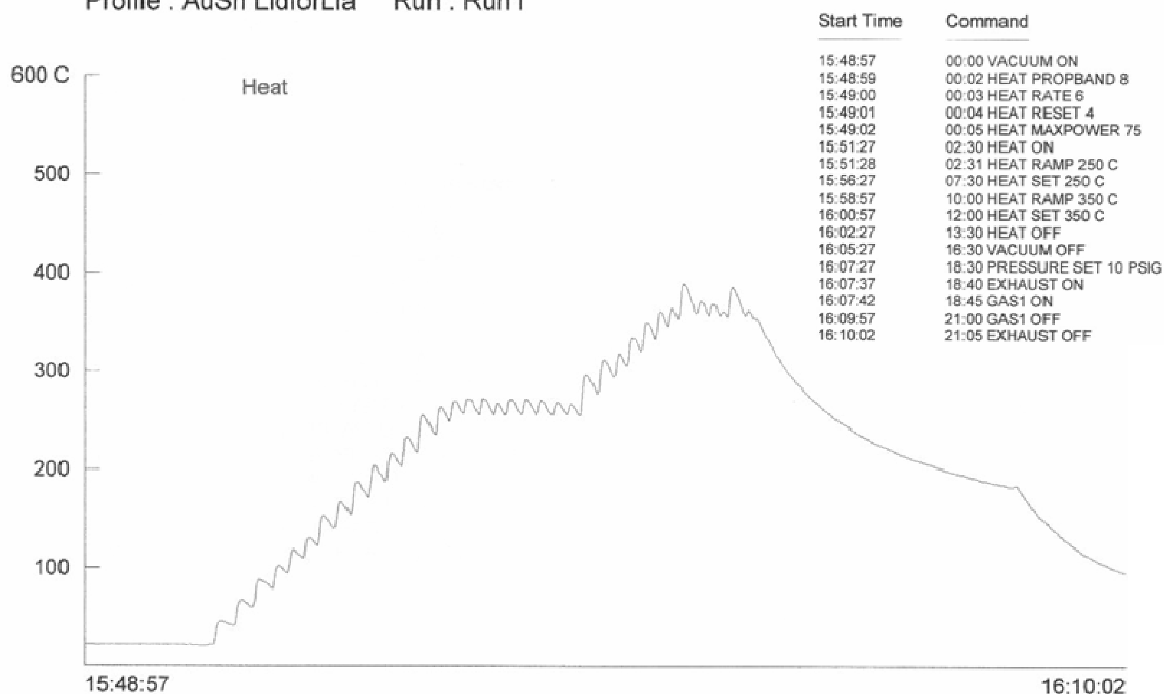

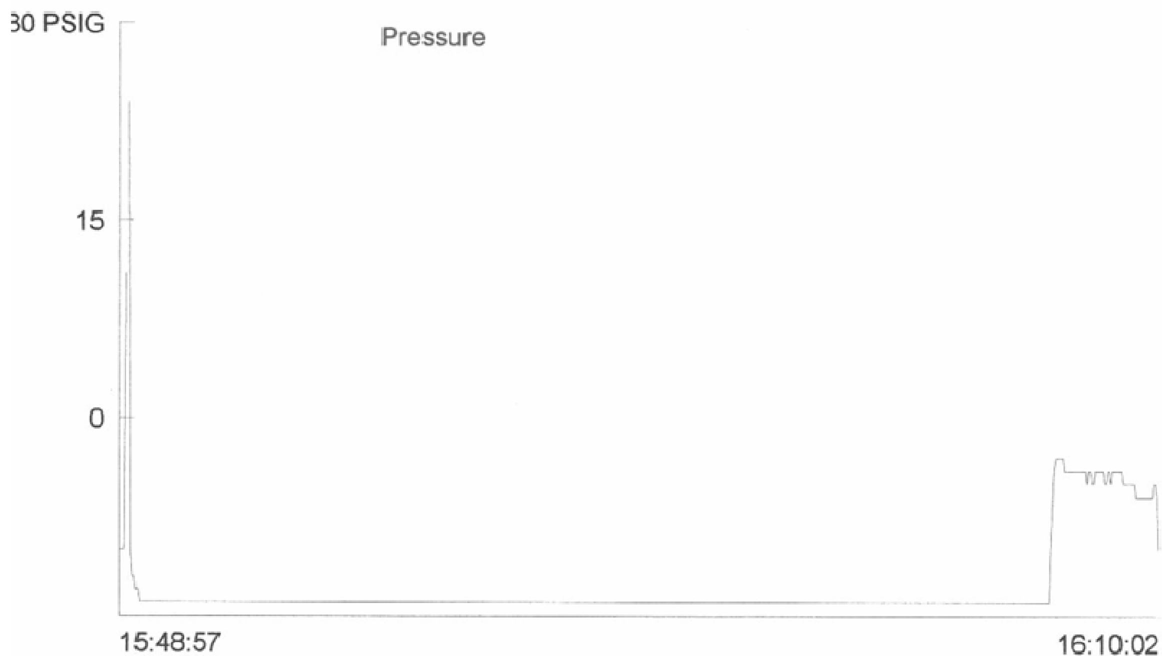

Figure 3-15 Lid placement run profile used for the SST International 3150.

CHAPTER 4 MEMS RELAY CONTACT MODELING

The contact of surfaces has been extensively studied for more than half a century. Enhanced understanding of how surfaces behave thermally, electrically, and in terms of friction and wear is achievable by modeling surface contact performance. When two rough surfaces are in contact, only the peaks of the asperities are in contact; therefore the real area of contact is much less than the nominal area. The peaks of the asperities carry very high loads because of that, and thus are subject to yielding. For the MEMS relay, it was shown in Chapter 3 that the initial yielding and shakedown of the peaks of the asperities on the contact surface initially decreases the resistance, but eventually, after hundreds of thousands of contact cycles, the breakdown of the surface results in very high resistances causing the MEMS relay to fail.

Greenwood and Williamson (GW) [40] introduced one of the first models of elastic rough surface contact, by using the Hertzian solution for individual asperities and a Gaussian height distribution to describe their heights. Some assumptions of the GW model are that there is no deformation of the bulk material below the asperities and that there is no interference between adjacent asperities. Elasto-plastic models have been developed after that, such as the CEB model by Chang et al. [41] that uses volume conservation to model a partially plastically deformed hemisphere. Also there is the Kogut et al. [42] KE model that provides empirical expressions for contact force and area, and a detailed analysis of the stress distribution in the contact area. A novel

statistical model has been introduced by Jackson and Green (JG) [43] that accounts for a varying geometrical hardness effect, and more recently a multi-scale model has been presented by Jackson and Streator (JS) [44].

This current understanding of contact behavior is now being applied to contact surfaces in MEMS. The reliability of MEMS is still an issue due to tribological challenges introduced by the small size of their structures. For instance, the ratio of area to volume becomes much larger as the scale is decreased. Hence, surface mechanics become even more important. In this chapter, the GW, the JG, and the multi-scale models were used to model the MEMS relay electrical contact resistance (ECR) and are compared with measured results.

4.1 Greenwood and Williamson elastic contact model

The GW elastic contact model [39] assumes that the contact is between a plane and a supposedly flat surface that has many asperities with spherically shaped peaks. The GW model also assumes that the radius of the peaks *R*, are the same, and the height of the asperities vary according to the Gaussian distribution shown by

$$\phi(z) = \frac{1}{2\pi\sigma_s}\exp\left[-\frac{1}{2}\left(\frac{z-\bar{z}}{\sigma_s}\right)^2\right] \tag{10}$$

Where σ_s is the standard deviation of the asperities heights, and is related to the roughness of the surface (σ) by McCool [45] as shown by

$$\sigma^2 = \sigma_s^2 + \frac{3.717x10^{-4}}{\eta^2 R^2} \tag{11}$$

McCool [45] also provides a methodology for finding the average radius of the peaks (R), and the area density of the asperities (η). The number of asperities on the surface n, is the nominal or apparent area of contact A_N (the surface where the asperities are scattered) multiplied by the area density of the asperities (η). The total number of asperities in contact is then the number of asperities multiplied by the probability of making contact at any given asperity as shown by

$$n = \eta A_n \int_d^\infty \phi(z) dz \tag{12}$$

Therefore, the total contribution from the asperities to the real area of contact, the total contact force, and the electrical resistance are found, as shown in Equations (13)-(15). The interference between surfaces $\omega = (z\text{-}d)$ is also the distance perpendicular to the surface the asperities compress when in contact. Where z is the height of asperity measured from the mean of asperity heights, and d is the separation of mean asperity height.

$$\frac{A_R}{A_N} = \eta \pi R \int_d^\infty (z-d)\phi(z) dz \tag{13}$$

$$\frac{W}{A_N E'} = \frac{4}{3} \eta R^{1/2} \int_d^\infty (z-d)^{3/2} \phi(z) dz \tag{14}$$

$$\frac{R^{-1}}{A_N} = 2\eta \rho^{-1} R^{1/2} \int_d^\infty (z-d)^{1/2} \phi(z) dz \tag{15}$$

Where

$$E' = \frac{E}{2 \cdot \left(1-\nu^2\right)} \tag{16}$$

4.2 Jackson and Green elasto-plastic hemispherical contact model

The GW model does not account for plastic deformations in the surface asperity. A recent model introduced by JG [43] that accounts for plastic deformation of the surface claims to be more accurate than later models. To introduce the plastic solution to the GW model, the JG model uses the critical interference ω_c, the point where yielding begins to occur between the surfaces. Jackson and Green [46] applied the von Mises yield criterion to derive the critical interference, as shown in by

$$\omega_c = \left(\frac{S_y C \pi}{2E'} \right)^2 R \qquad (17)$$

where

$$C = 1.295\left(\exp(0.736\nu)\right) \qquad (18)$$

This model assumes that there is no friction between the surface and the sphere. In actuality, the friction may have an effect on the area of contact predicted from the model. For the region where $0 \leq \omega/\omega_c \leq 1.9$, the Hertzian single asperity model should be used. The elastic perfectly plastic solution from JG should be used for the region where $\omega \geq 1.9\, \omega_c$. Following the same idea shown in the previous section, the total area of contact (Equation (19)), and the total load (Equation (20)), are derived.

$$\frac{A_R}{A_N} = \eta \pi R \int_d^{\infty} \omega \cdot \left(\frac{\omega}{1.9\omega_c} \right)^B \phi(z) dz \qquad (19)$$

$$\frac{W}{A_N E'} = \frac{\eta \overline{P_c}}{E'} \int_d^{\infty} \left[\left(\frac{\omega}{\omega_c} \right)^{3/2} \exp\left[-\frac{1}{4} \left(\frac{\omega}{\omega_c} \right)^{5/12} \right] + \frac{4H_G}{CS_y} \left(\frac{\omega}{\omega_c} \right) \left\{ 1 - \exp\left[-\frac{1}{25} \left(\frac{\omega}{\omega_c} \right)^{5/9} \right] \right\} \right] \phi(z) dz \qquad (20)$$

where:

$$\overline{P}_c = \frac{4}{3}\left(\frac{R}{E'}\right)^2\left(\frac{C}{2}S_y\pi\right)^3 \tag{21}$$

and $\overline{P}_c$ is the critical contact force at initial yielding

$$B = 0.14\exp\left(23\cdot\frac{S_y}{E'}\right) \tag{22}$$

$$\frac{H_G}{S_y} = 2.84\left[1-\exp\left(-0.82\left(\sqrt{\frac{\omega}{R}}\left(\frac{\omega}{1.9\omega_c}\right)^{B/2}\right)^{-0.7}\right)\right] \tag{23}$$

For the elasto-plastic solution, the radius of the contact is shown in Equation (24)

$$a = \sqrt{D\omega R} \tag{24}$$

Where $D = 1$ for $0 \le \omega/\omega_c \le 1.9$, and $D = \left(\frac{\omega}{1.9\omega_c}\right)^B$ otherwise. From these equations, the total resistance across the contact can be modeled as shown in Equation (25).

$$\frac{R^{-1}}{A_N} = 2\eta\rho^{-1}R^{1/2}\int_d^{\infty}\left(\frac{\omega}{1.9\omega_c}\right)^{B/2}\omega^{1/2}\phi(z)dz \tag{25}$$

For the JG model the statistical model used is the full Gaussian distribution as shown in Equation (26).

$$\phi(z) = \frac{1}{\sqrt{2\pi}\sigma_s}\exp\left[-\frac{1}{2}\left(\frac{z}{\sigma_s}\right)^2\right] \tag{26}$$

As opposed to the KE model [41], the JG model accounts for material and geometry effects. The ω_c and $\overline{P}_c$ are dependent on yield strength, and thus indirectly depend on hardness. This is important because as shown by Jackson and Green [46],

hardness changes with surface geometry. Therefore, in this model, Equation (23) is used to predict the hardness as a function of the contact material properties and geometry.

4.3 Multi-scale model

Surfaces have several levels of roughness; they are multi-scale in nature. One approach to handling the multi-scale nature of surface roughness was offered by Majumdar and Bhushan (MB) [47] and others [48]-[51], who developed a fractal based descriptions of surface contact. An innovative iterative multi-scale model that also attempts to address this issue has been developed by Jackson and Streator [44]. The current work will make use of this multi-scale model to predict the real area of contact and hence, the electrical contact resistance for the MEMS relay.

The same direction of thought as Archard [55] is used in the multi-scale model [44] but provides a method that can be easily applied to real surfaces. Following the model assumptions given in [44] results in a simple framework of equations for the contact model:

$$A_r = \left(\prod_{i=1}^{i_{\max}} \overline{A}_i \eta_i \right) A_n \tag{27}$$

$$F = \overline{F}_i \eta_i A_{i-1} \tag{28}$$

where A_r is the real area of contact, the subscript i denotes a frequency level with $i_{\max}$ denoting the highest frequency level considered, $\overline{A}_i$ and η_i are the single asperity contact area and the areal asperity density level, respectively, and A_n is the nominal (total) contact area. F is the contact load, and $\overline{F}_i$ is the single asperity contact force at a given

frequency. For a simplified example, if there are only two frequency levels of asperities Equation (27) becomes

$$A_r = \overline{A}_2 \eta_2 \overline{A}_1 \eta_1 A_n \tag{29}$$

The number of asperities at frequency level 1 is the areal asperity density of the first frequency times the nominal area ($\eta_1 A_n$). Therefore, the number of asperities at frequency level 1 times the single asperity contact area of frequency level 1 ($\overline{A}_1 \eta_1 A_n$) is the nominal contact area from the perspective of level 2. Subsequently, the real contact area (A_r) is given by multiplying the number of asperities at frequency level 2 ($\eta_2 \overline{A}_1 \eta_1 A_n$) by the asperity contact area of level 2 ($\overline{A}_2$). Values for the single asperity contact area per frequency level are determined from a selected micro-contact model (e.g., Hertz), with the assumption that at a given level, the contact load is equally shared by all asperities, with the asperity radius of curvature established from the frequency spectrum. Generally, the cycle described in the example above continues until all the asperity frequency levels are considered. Hence, the real area of contact between two rough surfaces is found by using a recursive approach.

After selecting the scan length (L), the input surface data is acquired using techniques such as optical microscopy, electron microscopy, or surface profilometry and an FFT is performed on it. From the resulting Fourier series, the asperity areal density and radius of curvature are computed for each frequency level according to:

$$\eta_i = 2 f_i^2 \quad (30)$$

$$R_i = \frac{1}{4\pi^2 \beta_i f_i^2} \quad (31)$$

Where f_i denotes the frequency (i.e., the reciprocal of wavelength) and β_i is the amplitude corresponding to the given frequency. The nominal contact area (A_n) is then set to be equal to L^2 and is identified with $i = 0$. Additional details of the model can be found in Jackson & Streator [44]. The contact resistance is included in the multi-scale model as described in the next section.

4.3.1 Asperity Electrical Contact Resistance

The highest frequency level that reduces the area of contact for the MEMS relay has a calculated asperity radius, R_i, of approximately 1 μm. The resistance can then be modeled using the Maxwell spreading resistance formula [58], for two gold surfaces (ρ = $2.20 \cdot 10^{-8}$ Ω·m)

$$R_{asp} = \frac{\rho}{2a} \quad (32)$$

The total electrical contact resistance between the surfaces at the highest frequency level that reduces the area of contact is given by

$$R_c = \frac{R_{asp}}{\eta_i A_{i-1}} \quad (33)$$

where $\eta_i A_{i-1}$ is the number of asperities (N) at the highest frequency level that reduces the contact area.

In the present study, the multi-scale model is used in combination with either the Hertzian model [56] at the asperity level to model elastic contact; whereas to model

elasto-plastic contact, the multi-scale framework is used in conjunction with the asperity deformation model of Jackson and Green (JG) [43].

4.4 Results and Discussion

The MEMS relay surface roughness was measured using a Wyco optical profilometer with a field of view of 420 µm x 420 µm. The acquired leveled surface roughness data is shown in Figure 4-1. The contact surface is composed of electroplated gold (Figure 4-2). The material and surface properties used to implement the GW, JG models is shown in Table 4-1.

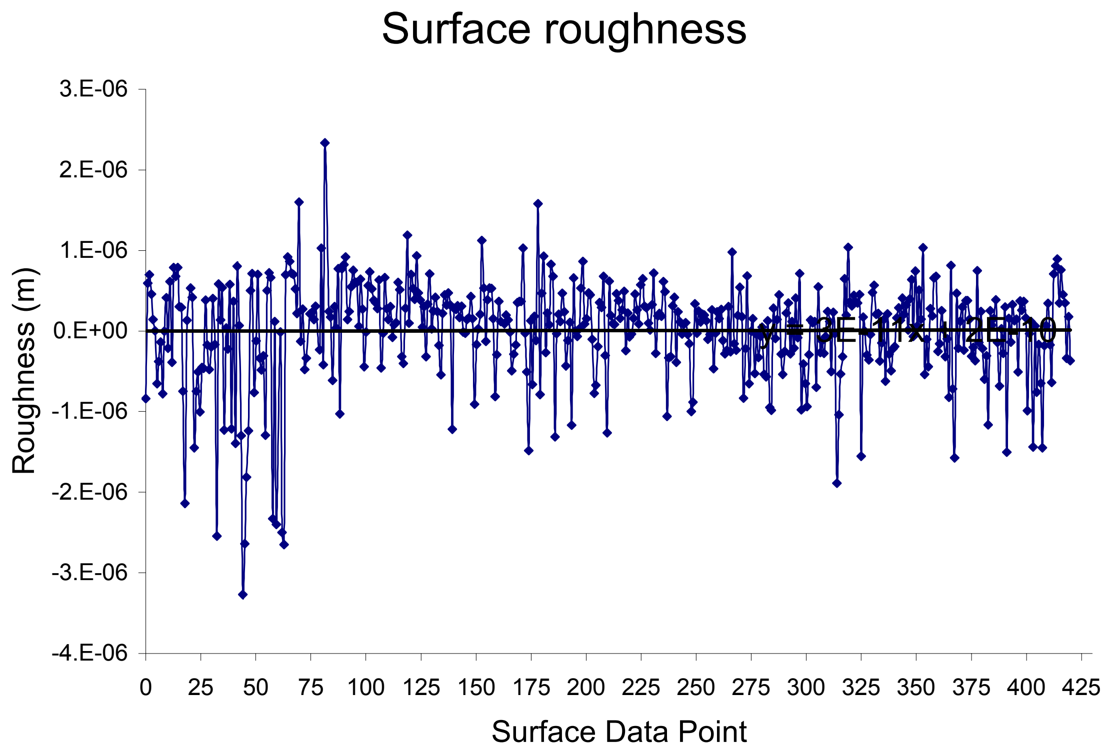

Figure 4-1 Suface data for MEMS relay contact surface acquired using the Wyco optical profilometer.

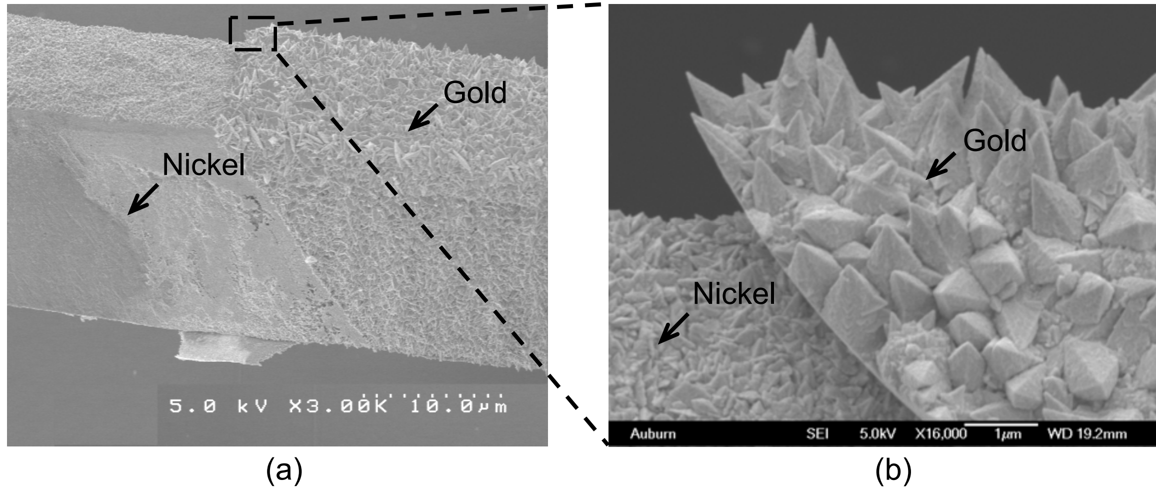

Figure 4-2 SEM picture of the contact surface of the MEMS relay a) contact finger showing 1 μm thick gold electroplated on nickel, and b) a portion of the finger showing the rough gold contact surface on nickel.

Table 4-1 Material and surface properties for MEMS relay

Elastic Modulus (E) = 77.2 GPa	Std. Deviation of Surface Heights (σ) = 0.633 μm
$E'=E/(2*(1-v^2))$ = 46.9 GPa	Std. Deviation of Asperity Heights (σ_s) = 0.439 μm
Poisson's Ratio (v) = 0.42	Radius of Hemispherical Asperities (R) = 1.365 μm
Yield Strength (S_y) = 120 MPa	Area Density of the Asperities (η) = 3.10 x 10^{10} m^{-2}
Critical Interference (ω_c) = 6.87 x 10^{-11} m	Critical Pressure ($\overline{P}_c$) = 4.16 x 10^{-8} Pa

The GW and JG models discussed in sections 4.1 and 4.2 were solved assuming a rough surface contacting a smooth plane. Figure 4-3 shows the plot of the real contact area (*Ar)* versus the load (*F*). From the plot it can be noted that as predicted, as load increases, the contact area also increases. The resistance of the contacts has the opposite relationship with load as expected; it decreases with increasing loads, because as the area increases, the resistance becomes less. The resistance versus dimensionless load is shown in Figure 4-4. For both the area and the resistance, the JG values are ten times larger than GW values for a chosen load. For the load range applied to the MEMS relay during testing, it can be noted that the JG resistance model is very accurate in predicting the resistance of the MEMS relay.

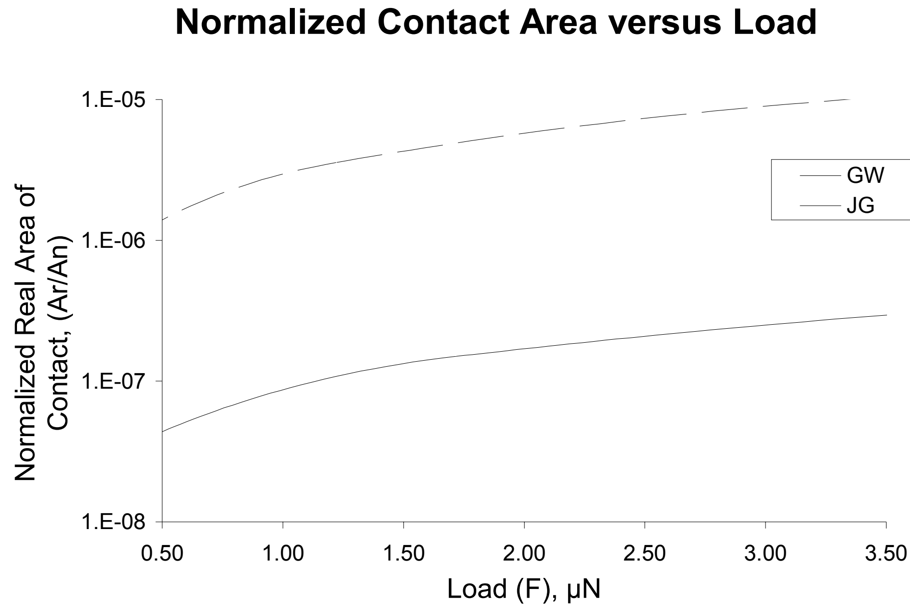

Figure 4-3 Comparison between the GW and the JG models for contact area versus load

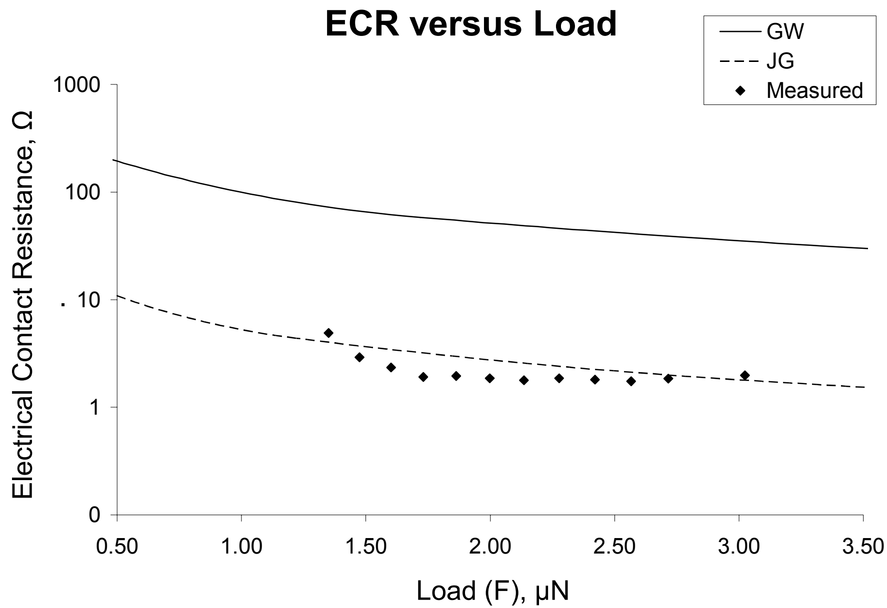

Figure 4-4 Comparison between the GW, JG models, and measured results for ECR versus load

The multi-scale model discussed in section 4.3, was solved using both the Hertzian, and the JG models, for a surface data that reflects contact between two rough

surfaces. The ECR versus load for the multi-scale model is shown in Figure 4-5. The multi-scale model over predicts the resistance of the MEMS relay.

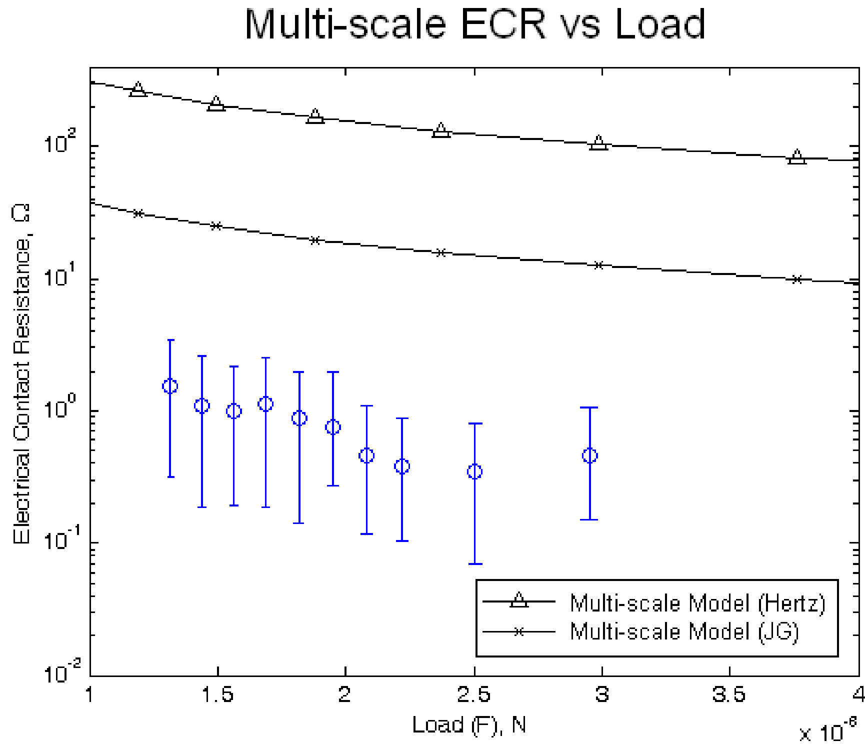

Figure 4-5 Comparison between the Hertz and JG multi-scale models and measured results for the MEMS relay

In this chapter, the modeling of the MEMS relay contact surface was presented. The Jackson and Green statistical model is shown to have very good agreement with the measured electrical contact resistance. The other models such as the Greenwood and Williamson statistical model and the Hetzian and the Jackson and Green multi-scale models show good qualitative agreement, but they over predict the electrical contact resistance. In the next chapter, a summary of the results offered in this thesis along with suggestions for improvements and future work are presented.

CHAPTER 5 SUMMARY AND FUTURE WORK

5.1 Summary

A novel MEMS relay fabricated using MetalMUMPs is presented in this thesis. MEMS relays exhibits advantages over semiconductor based switches such as low loss, low power consumption, and absence of intermodulation distortion. A major shortcoming of MEMS relays is reliability. Stiction and resistance degradation are major factors that limit the reliability of MEMS relays. The study of MEMS relays characteristics enables a better understanding of the causes for the poor reliability of these devices.

5.2 Design, Simulation and Fabrication

A MEMS relay composed of two comb drives, a folded suspension spring, and ten contact fingers was designed. Simulation of the design was done using CoventorWare™ [33]. The simulation results were very similar to the theoretical calculations. MetalMUMPs process [30] was successfully used to fabricate the MEMS relay.

5.3 Experimental Characterization and Packaging

The resistance versus voltage characteristics have been measured in the voltage range of 172 V to 220 V, for a few different contact designs. The average resistance of

the MEMS relays range from 0.2 Ω to 1.1 Ω. Dehydration experiments have been performed to avoid stiction caused by humidity. Lifetime of two relay designs have been presented for up to $1x10^6$ actuation cycles. Some initial work in packaging the MEMS relay has been presented.

5.4 Modeling

The comparison between the GW and the JG models, shows that the elasto-plastic solution accounts for the deformation of the asperity peaks, and therefore yields a larger real contact area per load value. The JG resistance model shows very good agreement to measured results. For the multi-scale case, two rough surfaces are in contact, and the results show good qualitative agreement with measured results.

5.5 Future Work

Most of the study of the MEMS relay presented in this thesis was done for flat contact surfaces. Data should be collected for several other MEMS relays in order to have results that are statistically sound. Other contact geometries should also be studied (resistance versus voltage and reliability), in order to determine the geometry that delivers the best performance.

The contact surfaces studied have a gold layer. Other metals could be used to achieve better performance. The performance of the gold contact could be compared with that of Nickel. Also, the presence of hydrocarbon films formed on top of the gold has been reported [57], which could explain why the 4-wire multimeter does not show a resistance when a voltage between 120V and 170V is applied, even though there is

contact. A study could be performed of current versus voltage across the contact in order to better define the role of the hydrocarbon in the performance of the MEMS relay.

The packaging of the MEMS relay could be done with several different gases, as well as vacuum, and their characteristics compared. Also testing of the packaged MEMS relay under different conditions such as high temperatures, and humidity could be performed.

BIBLIOGRAPHY

[1] I.J. Bahl and P. Bhartia (Eds.), *Microwave Solid State Circuit Design*, John Wiley & Sons, New York, pp. 771-850, Second Edition, April 2003.

[2] S. E. Alper, T. Akin, "A Single-Crystal Silicon Symmetrical and Decoupled MEMS Gyroscope on an Insulating Substrate," J. Microlectromechanical Systems, vol 14, no 4, pp 707-717, 2005.

[3] K. Subramanian, J. B. Fortin, K. Kishore, "3-Dimensional Scalable Pressure Sensors: Dvice and Process Design," Proc. of IEEE Sensors, vol. 1, pp 531-534, 2004.

[4] L. P. Wang, et al, "Microelectromechanical Systems (MEMS) Accelerometers Using Lead Zirconate Titanate Thich Films," IEEE Electron Device Letters, vol. 23, no. 4, 2002.

[5] K. E. Petersen, "Dynamic Micromechanics on Silicon: Techniques and Devices," IEEE Trans. Electron. Devices, vol. 25, no. 10, Oct. 1978.

[6] K. E. Petersen, "Micromechanical Membrane switches on silicon," IBM J. Res. Develop., vol. 23, no. 4, pp. 376-385, July 1979.

[7] H. J. De Los Santos, *Introduction to Microelectromechanical Microwave Systems*, Artech House, MA, 1999.

[8] G. M. Rebeiz, *RF MEMS: Theory, Design, and Technology*, John Wiley & Sons, NJ, 2002.

[9] Kai. M. Hiltman, Bertram Schmidt, Hermann Sandmaier and Walter Lang, "Development of Micromachined switches with increased reliability," Transducers, pp. 1157-1160, 1997.

[10] S. Majumder, N. McGruer, G. Adams, P. Zavracky, R. Morrison, and J. Krim, "Study of contacts in an electrostatically actuated microswitch," Sensors and Actuators A 93, pp 19-26, 2001.

[11] S. Majumder, N. McGruer, and G. Adams, “Adhesion and Contact Resistance in an Electrostatic MEMS Microswitch,” Contact Mechanics - Friction: Modeling and Experiment, pp 79-84, 2003.

[12] P. Zavracky, S. Majumder, and N. McGruer, “Micromechanical Switches Fabricated Using Nickel Surface Micromachining,” J. Microelectromech. Syst., vol. 6, no. 1, pp. 3-9, Mar. 1997.

[13] D. Hyman and M. Mehregany, “Contact Physics of Gold Microcontacts for MEMS Switches,” IEEE Trans. Comp. Packag. Technol., vol. 22, no. 3, pp. 357-364, Sept. 1999.

[14] S. Roy, and M. Mehregany, “Design, Fabrication, and Characterization of Electrostatic Microrelays,” SPIE Micromachined Devices and Components Vol. 2642, pp. 64-73, Sept. 1995.

[15] R. Chan, R. Lesnick, D. Becher, and M. Feng, “Low-Actuation Voltage RF MEMS Shunt Switch With Cold Switching Lifetime of Seven Billion Cycles,” J. of Microelectromech. Syst., vol. 12, no. 5, pp. 713-719, Oct. 2003.

[16] D. Becher, R. Chan, M. Hattendorf, and M. Feng, “Reliability Study of Low-Voltage RF MEMS Switches,” GaAsMANTECH Conference, 2002

[17] B. McCarthy, G. Adams, N. McGruer, and D. Potter, “A Dynamic Model, Including Contact Bounce, of an Electrostatically Actuated Microswitch,” J. of Microelectromech. Syst.,vol. 11, no. 3, pp. 276-281, June 2002.

[18] J. DeNatale, R. Mihailovich, and J. Waldrop, “Techniques for Reliability Analysis of MEMS RF Switch,” IEEE 40th Annual Int. Reliability Physics Symposium, pp 116-117, Dallas, Texas, 2002.

[19] J. Maciel, “Recent Reliability Results in RF MEMS,” at the workshop “WFE: Recent Applications of RF MEMS”, IEEE MTT-S International Microwave Symposium, Long Beach, CA, June 17, 2005.

[20] W. Merlijn van Spengen, R. Puers, and I. De Wolf, “The Prediction of Stiction Failure in MEMS,” IEEE Trans. On Devices and Materials Reliability, vol. 3, no. 4, pp. 167-172, Dec. 2003.

[21] D. Hyman et al., “Surface-micromachined RF MEMs switches on GaAs substrates,” Int. J. of RF and Microwave CAE, vol. 9, no. 4, pp. 348-361, 1999.

[22] J. J. Yao and M. F. Chang, "A surface micromachined miniature switch for telecommunications applications with signal frequencies from DC up to 4 GHz," Tech. Digest of 8th Int. Conf. on Solid-State Sensors and Actuators, pp. 384-387, 1995.

[23] Guan-Leng Tan, G. M. Rebeiz, "A DC-Contact MEMS Shunt Switch," IEEE Microwave and Wireless Components Letters, Vol. 12, No. 6, pp. 212-214, June 2002.

[24] M. -A. Gretillat, F. Gretillat, and N. F. de Rooji, "Micromechanical relay with electrostatic actuation and metallic vontacts," J. of Micromech. Microeng., vol. 9, pp. 324-331, 1999.

[25] L.E Larson, R. H. Hackett and R.F. Lohr, "Microactuators for GaAs-Based microwave integrated circuits," IEEE MTT-S Int. Microwave Symp. Dig., pp. 743-746, June 1991.

[26] E. J. J. Kruglick and K. J. Pister, "Lateral MEMS microcontact considerations," J. of IEEE Microelectromechanical Systems, vol. 8, pp. 264-271, 1999.

[27] I.Schele and B.Hillerich, "Comparison of lateral and vertical switches for application as microrelays," J. of Micromech. Microeng., vol. 9, pp. 146-150, 1999.

[28] Z. Li, D. Zhang, T. Li, W. Wang, and G. Wu, "Bulk micromachined relay with lateral contact," J. Micromeh. Microeng., vol. 10, pp 329-333, 2000.

[29] J. D. Irwin and R. M. Nelms, *Basic Engineering Circuit Analysis*, John Wiley & Sons, New York, Seventh Edition, May 2006.

[30] A. Cowen, B. Dudley, E. Hill, M. Walters, R. Wood, S. Johnson, H. Wynands, and B. Hardy, MetalMUMPs Design Handbook, MEMSCAP revision 1.0, 2002.

[31] S. D. Senturia, *Microsystems Design*, Springer, New York, First Edition, November, 2000.

[32] M. Gad-el-Hak, *The MEMS Handbook*, CRC Press, Florida, Second Edition, December, 2005.

[33] CoventorWare™ Ver. 2005, Coventor Inc, NC, USA

[34] M. Bakri-Kassem and R. R. Mansour, Two Movable Plate Nitride Loaded MEMS Variable Capacitor, *IEEE Trans. Microwave Theory Tech.*, MTT-52, pp. 831- 837, 2004.

[35] K. Leedy, R. Cortez, J. Ebel, R. Strawser, and A. Walker, “Metallization scheme for radio frequency microelectromechanical system switches,” J. Vac. Sci. Technol. A 21(4), Jul/Aug. 2003.

[36] Srolovitz, David J.; Cha, Pil-Ryung; Kim, Ji-Hee; Song, Jun, “Evolution of asperity contacts,” JOM, v 56, n 11, pp 89, November, 2004.

[37] J. Song, P. Cha, D. Srolovitz, “Molecular dynamics study of mutli-cycle single asperity contact,” JOM, v 56, n 11, p 12, November, 2004.

[38] C. B. O’Neal et al, “Challenges in the Packaging of MEMS,” Int. Symp. on Adv. Packaging Mat., pp 41-47, 1999.

[39] T. R. Hsu, *MEMS Packaging,* The IEE INSPEC, UK, 2004

[40] J. A. Greenwood, J. B. Williamson, “Contact of nominally flat surfaces,” Proc R Soc Lond A, vol 295, pp 300-319, 1966.

[41] W. R. Chang, I. Etsion, D. B. Bogy, “An elastic-plastic model for the contact of rough surfaces,” ASME J Tribol, vol 109, pp 257-263, 1987.

[42] L. Kogut, I. Etsion, “Elastic-plastic contact analysis of a sphere and a rigid flat,” ASME J Appl Mech Trans; vol 69, no 5, pp 657-662, 2002.

[43] R. Jackson, I. Green, “A statistical model of elasto-plastic asperity contact between rough surfaces,” Trib Intl. vol 39, pp 906-914, 2006.

[44] R. Jackson, J. Streator, “A multi-scale model for contact between rough surfaces,” Wear, In Press, 2006.

[45] J. I. McCool, “Comparison of models for the contact of rough surfaces,” Wear, vol 107, pp 37-60, 1986.

[46] R. Jackson, I. Green, “A finite element study of elasto-plastic hemispherical contact,” ASME J Tribol vol 127, pp 343-354, 2005.

[47] Majumdar, A. and B. Bhushan, “Fractal Model of Elastic-plastic Contact Between Rough Surfaces.” *ASME J. of Tribol*., vol 113(1), pp 1-11, 1991.

[48] Majumdar, A. and B. Bhushan, “Role of fractal geometry in roughness characterization and contact mechanics of surfaces.” *ASME J. of Tribol*., vol 112(2), pp 205-216, 1990.

[49] Warren, T.L. and D. Krajcinovic, “Fractal Models of Elastic-perfectly Plastic Contact of Rough Surfaces Based on the Cantor Set.” *International Journal of Solids and Structures*, vol 32(19), pp 2907-2922, 1995.

[50] Willner, K., “Elasto-plastic Normal Contact of Three-dimensional Fractal Surfaces Using Halfspace Theory.” *ASME J. of Tribol*., vol 126(1), pp 28-33, 2004.

[51] Yan, W. and K. Komvopoulos, “Contact Analysis of Elastic-Plastic Fractal Surfaces.” *Journal of Applied Physics*, vol 84(7), pp 3617-3624 1998.

[52] Greenwood, J.A. and J.B.P. Williamson, “Contact of Nominally Flat Surfaces.” *Proc. R. Soc. Lond. A*, vol A295, pp 300-319, 1966.

[53] Majumdar, A. and C.L. Tien, “Fractal Characterization and Simulation of Rough Surfaces.” *Wear*, vol 136(2), pp 313-327, 1990.

[54] Kogut, L., Jackson, R. L., “Comparison of Elastic Contact Modeling Utilizing Statistical and Fractal Approaches,” *Journal of Tribology, Trans. ASME*, vol 128(1), pp 213-217, 2005.

[55] Archard, J.F., “Elastic Deformation and the Laws of Friction. “Proc. R. Soc. Lond. A, vol 243, pp 190-205, 1957.

[56] Timoshenko, S., and Goodier, J. N., *Theory of Elasticity*. McGraw-Hill, New York, 1951.

[57] A. Frischknecht, B. Jensen, ‘*Influence of Heat, Force, and Secondary Factors on Electrical Contact Resistance in Microscale Gold Contacts,”* Int. Joint Trib. Conf, San Antonio, TX, Oct. 2006.

[58] R. Holm, *Electrical Contacts*, 1967, New York: Springer.

APPENDICES

APPENDIX A AMSTC MEMS RELAY FABRICATION

A.1 Introduction

Initially, several attempts were made to manufacture the MEMS relay described in this thesis at the Alabama Microelectronics Science and Technology Center (AMSTC). At the same time a modified design was submitted to MetalMUMPs. Because the MEMS relay was successfully manufactured using MetalMUMPs, further attempt to fabricate at AMSTC was not pursued. In this appendix, the process used for fabricating the MEMS relay at AMSTC is described.

A.2 Design

The design was done by using the same formulas described in Chapter 2. For this design regular springs were used instead of the folded spring. The relay designed to be fabricated at AMSTC had much smaller features than the design later developed to be manufactured using MetalMUMPS. A few design features include 200 µm spring length, and 2 µm spring width. For the comb drive, 4 µm comb fingers, and 3 µm gap between comb fingers; and a gap between the relay contact surfaces of 10 µm. The masks designed to manufacture the relay are described in this section.

A.2.1 Mask Design

There were three masks designed to manufacture the relay. The first mask 'PADS mask' was used to define the aluminum/nickel pads for testing the relay. The second mask 'ANCHOR mask' was used to define the anchors as well as the sacrificial layer. The third mask 'NICKEL mask' was used to define the mold for electroplating the Nickel to form the relay. The mask levels for the multi and single contact relays are shown in Figure A- 1 and Figure A- 2, where the PADS mask is the same for both cases.

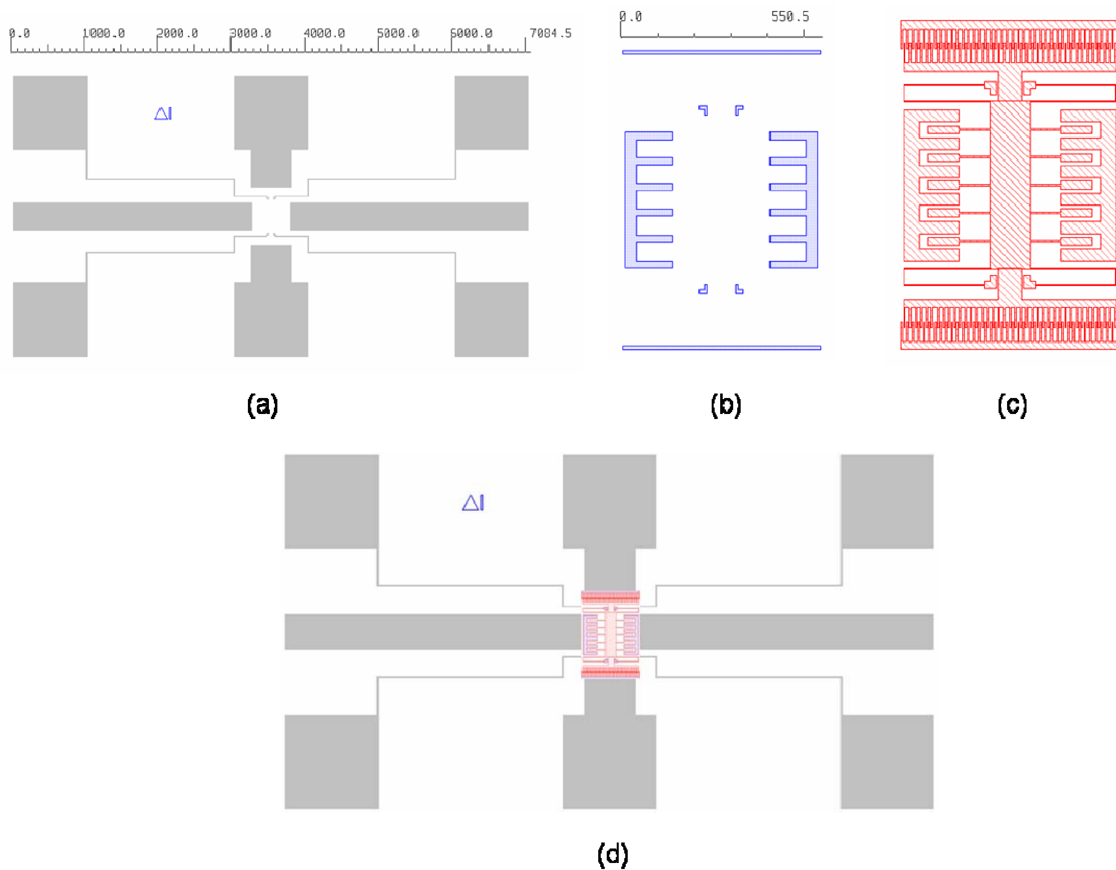

Figure A- 1 AMSTC fabrication masks for multi-contact design, (a) PADS, (b) ANCHOR, (c) NICKEL, and (d) all mask levels combined.

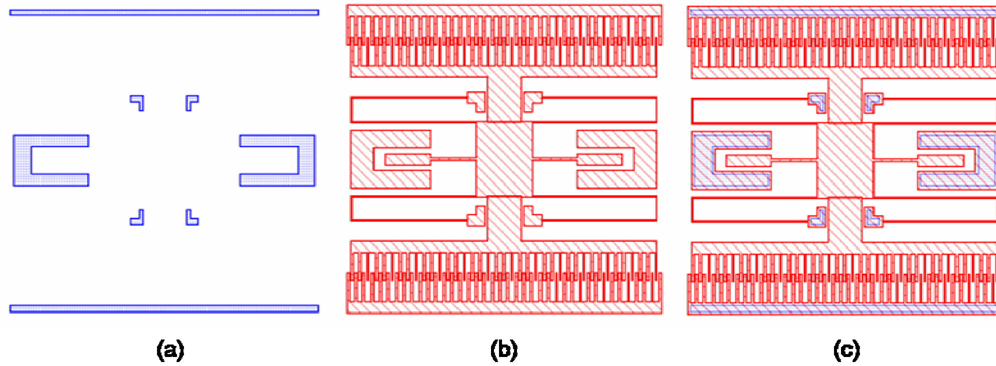

Figure A- 2 AMSTC fabrication masks for single-contact design, (a) ANCHOR, (b) NICKEL, and (c) ANCHOR and NICKEL levels combined.

A.3 Fabrication Process

In this section the processing steps are described below:

1. Start with a silicon substrate
2. Grow 1 µm thick insulating thermal oxide SiO_2 on the silicon substrate
3. Deposit 0.5 µm thick aluminum and 1 µm thick Nickel using e-beam
4. Spin coat AZ 5214 photoresist (available from Clariant Corporation) and pattern pads:
    a. Perform cleaning procedure:
        i. Spray acetone/methanol/DI water, dry wafer
        ii. Dehydrate the wafer using oven at 120ºC for approximately 20 min
        iii. Apply HMDS by evaporation for 13 minutes
    b. Spin wafer for 30 sec at 3000 rpm and apply photoresist
    c. Soft bake wafer using hot plate for 1 min at 105ºC
    d. Expose using the mask aligner and the PADS mask for 6 sec

e. Develop for approximately 1 min using AZ 400K (available from Clariant Corporation) solution at 1 part of solution to 2 parts of DI water
f. Hard bake at 112ºC for 2 min
g. Etch nickel (300 ml Nitric/300 ml Acetic/150 ml Sulfuric/ 1050 ml DI)
h. Etch aluminum (PAE)
i. Remove photoresist using O_2 Plasma, in the Matrix (1 min at 300 Watts)

5. Use STR 1045 photoresist (available from Shipley) as the release layer. The processing steps for 1045 are as follows:
   a. Perform cleaning procedure
   b. Spin wafer for 30 sec at 1500 rpm and apply STR 1045 photoresist
   c. Soft bake using a 90 º C oven for 35 min, wafer should be leveled with photoresist facing up
   d. Using the mask aligner and the ANCHOR mask, align and expose for 35 seconds
   e. Develop for 3.5 min using 1 part of 400K developer to 4 parts of DI water
6. In order to make the STR 1045 resistant to the solvents used in the SU-8 processing, the 1045 photoresist was gradually hard baked to very high temperatures and the details for hard baking are given below:
   a. Expose wafer using a blank mask for 30 sec to further cross link Photoresist and avoid flowing of the photoresist
   b. Bake in oven at 120ºC for 30 min
   c. Increase temp to 140ºC and bake for 30 min
   d. Increase temp to 160ºC and bake for 30 min

e. Increase temp to 180ºC and bake for 2 hours

f. Decrease the temperature of the oven to 120ºC and remove when the temperature reaches 120ºC and let the wafer cool down.

g. Thickness of photoresist at this point was 5.775 um

h. To make sure there is no photoresist left in the opening for the anchor, a 30 sec O_2 plasma cleaning at 500 Watts was used.

i. After plasma cleaning, the thickness of the photoresist release layer was measured to be 5 µm.

7. The seed layer (0.1 µm of Titanium and 0.5 µm of Copper, shown in Figure A- 3) for platting the relay was deposited using the e-beam A typical anchor opening for a single switch is shown in Figure A- 4 and Figure A- 5.

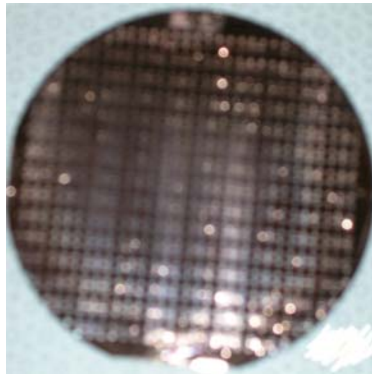

Figure A- 3 A 4” Wafer after Ti/Cu seed layer deposition.

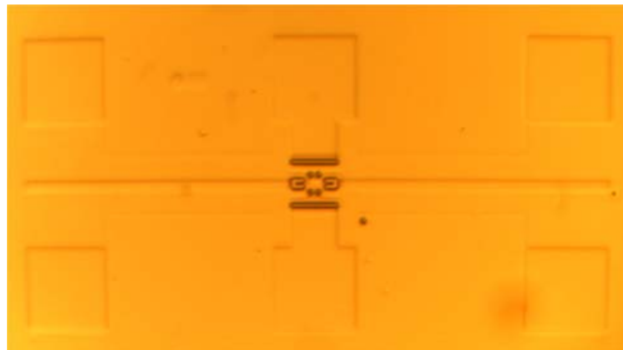

Figure A- 4 The anchor openings in the 1045 photoresist

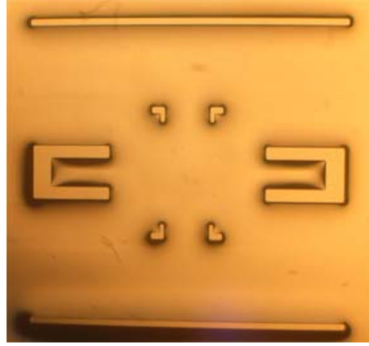

Figure A- 5 Close up view of anchor openings shown in Fig A-4.

8. The platting mold was defined using 15 μm thick SU-8 (available from MicroChem corp.) as shown in Fig. A-6. The processing steps are described below:
   a. Perform cleaning procedure described in part 4
   b. Spin coat Omnicoat (available from MicroChem Corp): step 1) 500 rpm for 5 sec, and step 2) 3000 rpm for 30 sec.
   c. Soft bake using hot plate for 1 min at 200ºC
   d. Spin coat 25 μm thick SU-8: step 1) 500 rpm for 5 sec, and step 2) 3000 rpm for 35 sec
   e. Make sure that hot plate is leveled.
   f. Soft bake using hot plate - start at 50ºC, ramp the temperature to 95ºC at 2.25ºC per minute and leave it for 7 min. Then, cool down wafer to room temperature (approximately one hour).
   g. Expose wafer using the mask aligner and the NICKEL mask for 34 seconds
   h. Post Exposure bake: Same procedure as Soft bake but leave the wafer at 95 ºC for 3 min instead of 7 min.
   i. Develop the wafer for 3 min using SU-8 developer
   j. O_2 plasma cleaning to remove the Omnicoat layer, 30 sec at 300 Watts.

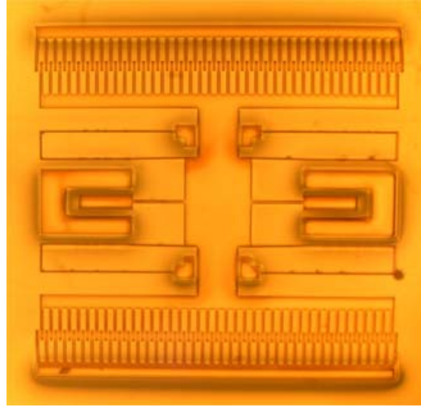

Figure A- 6. SU-8 mold for for plating the switch

9. Electroplating

The electroplating cell used consists of a nickel sulfamate solution (200 g/L-Nickel Sulfate, 5g/L of Nickel Chloride, 25 g/L of Boric Acid, 3 g/L of Saccharin), a nickel plate, the wafer to be platted, a power supply and an amp meter. The nickel plate and the wafer are placed in the solution facing each other. The negative terminal of the power supply is connected to the wafer. The positive terminal of the power supply is connected to the ammeter current terminal and the other terminal of the ammeter is connected to the nickel plate target.

The current required for platting depends on the total effective plating area. For an effective total platting area of 0.66 cm^2, the required current was calculated to be in the range of 1 to 2 mA corresponding to a desired current density of 1 mA/cm^2. The plating rate is proportional to the current density. In our experiment, the total plating time was about 3 hours. Once the desired 15 μm thickness was reached, the SU-8 was removed (Figure A- 7).

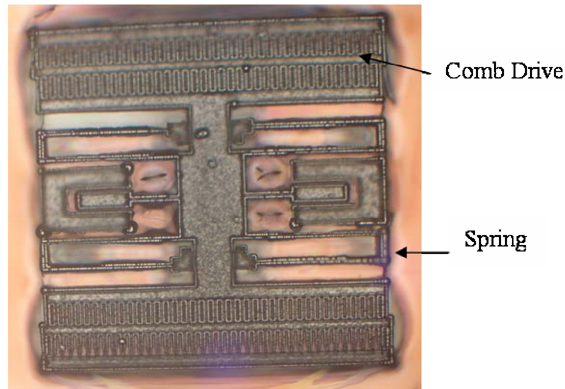

Figure A- 7. Electroplated nickel switches after removal of SU-8.

A.4 CONCLUSION

Initially, we patterned 25 μm thick SU-8. It was found that 2 micron wide features (namely, the width of the spring) are not feasible in this fabrication process. Subsequently, 15 micron thick SU-8 was spin coated and patterned as shown in Figure A-6 to reduce the aspect ratio and hence improve the fabrication process. A typical electroplated switch is shown in Figure A- 7. It was observed that the comb drive fingers were shorted due to the small spacing dimension (3 microns) between tall fingers (15 microns thick). It was concluded that this problem can be avoided in the next design by increasing the minimum feature size/spacing dimension to approximately 10 microns.

It was found that SU 8 does not stick well to copper. As a result, there was a lot of nickel platting underneath the SU-8. In order to avoid underplating, chromium could be deposited everywhere except where Nickel platting is desired (as shown in Figure A- 8). Because, Nickel does not plate to Chromium and SU 8 has better adhesion to Chromium.

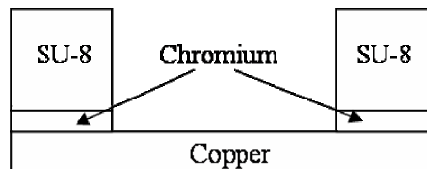

Figure A- 8 Suggestion to avoid nickel platting under SU-8.